Nearshore sediment pathways and potential sediment budgets in embayed settings over a multi-annual timescale

Nieves G. Valiente[a], Gerd Masselink[b], Robert Jak McCarroll[b], Tim Scott[b], Daniel Conley[b], Erin King[b]

[a] *Met Office, EX1 3PB, UK. Corresponding author at: FitzRoad Road, Exeter, Devon EX1 3PB, UK.*

E-mail address: Nieves G. Valiente (nieves.valiente@metoffice.gov.uk)

[b] *Coastal Processes Research Group, School of Biological and Marine Sciences, University of Plymouth, PL4 8AA, UK*

https://doi.org/10.1016/j.margeo.2020.106270

Keywords: nearshore sediment transport; headland bypassing; Delft3D.

Highlights

- Delft3D was used to investigate nearshore sediment transport dynamics
- Sediment budgets and potential headland bypassing rates over multi-annual timescales are predicted
- Bypassing sediment fluxes are episodic and can reach 10^4 m^3 day^{-1} over high energy conditions
- Hindcasted bypassing (10^3 – 10^5 m^3 y^{-1}) will affect coastal evolution over the decadal scale
- Magnitude of sub-tidal bypassing indicates substantial interconnectivity between cells previously thought limited to cross-shore oscillations

Abstract

Embayed beaches constitute a large proportion of the world's rocky coastlines, but there is a paucity of studies focusing on the longshore sediment exchange between embayed beaches separated by rocky stretches of coast. Here, we investigate the nearshore sediment transport dynamics along a 15-km stretch of the embayed coastline of north Cornwall, SW England, using Delft3D. Numerical simulations (coupled wave and tide) are conducted to compute major circulation modes and sediment fluxes, including order of magnitude for sediment bypassing between bays, for a wide range of modal and extreme wave conditions. Results indicate that extreme events cause (i) multi-embayment circulation and mega-rip formation where an alongshore current is deflected offshore (0.7 m s^{-1} at > 20 m depth) in the down-wave sectors, (ii) large bypassing rates (10^3– 10^4 m^3 day^{-1} bypassing) and (iii) exchanges extending to depths that exceed the base of the headlands. Accretionary phases over moderate-high swell periods were associated with clockwise intra-embayment circulation with simulated currents inducing redistribution towards the south in the long embayments (> 10^3 m^3 day^{-1} longshore). This circulation mode is combined with significant bypassing rates around the shallower and wider headlands (10^2 – 10^3 m^3 day^{-1}). Predictions of sediment fluxes along the lower shoreface are based on the correlation between the modelled sediment fluxes and offshore wave-conditions (r > 0.92), providing insights into the potential sediment budget over multi-annual timescales. Hindcasted yearly bypassing rates around the headlands range between 10^3 and 10^5 m^3 y^{-1} under an assumption of unlimited sediment supply, with the bulk of the transport occurring mainly during high energy events. Hence, the magnitude of the computed potential sediment fluxes presented here has implications for coastal evolution at longer timescales (>10 years), especially along sediment-starved coastlines.

1. Introduction

Embayed beaches constitute a large proportion of the world's rocky coastlines. Highly embayed beaches are often considered closed cells with the prominent headlands acting as barriers to littoral drift, such that sediment transport into and/or out of adjacent cells is insignificant. Consequently, there is a paucity of studies focusing on the longshore sediment exchange between embayed beaches separated by neighbouring rocky stretches of coast. Nevertheless, recent studies on sandy beaches show that important sediment transport pathways offshore and/or beyond the headlands may occur under particular conditions (Short, 2010; Aagaard, 2011; Goodwin et al., 2013; George et al., 2018; McCarroll et al., 2018; Vieira da Silva et al., 2018; King et al., 2019; Valiente et al., 2019a).

The physical coupling between the beach and the inner shelf is of major interest to coastal researchers, but key processes are still poorly resolved as this coupling is generally considered relatively limited. Recent observational studies of beach storm response and evolution emphasize that substantial transport occurs to large depths (George et al., 2018; Valiente et al., 2019b; McCarroll et al., 2019). Niedoroda and Swift (1981) showed that sediment may be permanently lost to the inner shelf during storms. Later, Wright et al. (1995) studied the surf zone processes connected to the inner shelf from a morphodynamic point of view, finding that part of the infragravity oscillations contributing to cross-shore transport and reaching the inner shelf area were originated in the surf zone. More recent studies of mega-rips and beach response to extreme storm events along embayed coastlines also point in this direction (Gallop et al, 2011; Loureiro et al., 2012; Castelle and Coco, 2013), revealing that a significant amount of sediment can be ejected outside the surf zone mainly due to the presence of mega-rips (Short, 2010; Castelle and Coco, 2013; McCarroll et al., 2016), and between adjacent beaches through headland bypassing (Duarte et al., 2014; McCarroll et al., 2018; Vieira da Silva et al., 2018). Short (1985) defined mega-rips as large-scale erosional rips which can reach up to 1 km offshore and occur when the headland\embayment topography forces wave refraction and surf zone longshore gradients. Moreover, largest alongshore sediment fluxes occur during large oblique waves (McCarroll et al., 2019). Along rocky coastlines, sediment transport may be disrupted and/or altered by the regional topography (e.g., embayment and headland configuration) introducing complexity in the general transport patterns that needs to be better understood.

For embayed coastlines, bypassing and embayment-scale cellular circulation involving mega-rips (Castelle et al., 2016) are the main mechanisms responsible for sediment exchange

between embayments and neighbouring areas. Based on observations, Gallop et al. (2011) and Loureiro et al. (2012) linked morphological change with embayment-scale circulation (rip and mega-rip formation) on several embayments of varying size and orientation. Additionally, Castelle and Coco (2013) studied the role of embayment morphometry in governing ejection outside the surf zone using simulations of passive tracers. They showed that the surf zone of embayed beaches systematically flushes out more floating material than on open beaches, with most exits occurring through the headland rips, and provided retention rates (in percentage) for varying beach length and constant headland length. More recent studies were more focused on the driving forces for sediment bypass around natural headlands. Vieira da Silva et al. (2018) investigated the influence of wind and waves on headland bypass whereas McCarroll et al. (2018) studied the role of embayment-scale circulation modes inducing bypass.

Sand bypassing rates are often predicted using simple analytical solutions such as one-line models on straight shorelines (Ab Razak et al., 2013; Brown et al., 2016). More sophisticated approaches include 2D and 3D process-based numerical modelling that is able to simulate horizontal and vertical currents. McCarroll et al. (2018) first introduced a site-specific bypass parameter for a multi-year period based on modelled sand bypassing rates on a single headland. A recent study by George et al. (2019) examined the impact of idealised headlands of varying size and shape on rates of headland bypass and determined that longshore sediment fluxes around headlands are mainly determined by the degree of blockage. However, despite these later efforts, prediction of sediment bypass in embayed beaches of different geometry and complex circulation remains poorly resolved.

A quantitative understanding of sediment pathways in littoral cells is fundamental when investigating beach response and evolution along embayed coastlines (Komar, 1998; Rosati, 2006; Thom et al., 2018). For closed cells, coastal changes need only be attributed to a redistribution of the sediment within the embayment, but for open or leaky cells, sediment exchanges within a larger area, including neighbouring embayments, need to be considered. Balances and imbalances between incoming and outgoing sediment fluxes encompassing several embayments, even when open, can ultimately provide essential information on the major sediment transport pathways, as well as help to derive sediment budgets within the inter-connected cells. Valiente et al. (2019b) followed a total sediment budget approach based on morphological observations in an embayed beach in SW England concluding that, despite the deeply embayed nature of the beach, the system was open. The approach allowed

quantification of sediment gains and losses; however, the understanding of the system was incomplete as it lacked information on the directional sediment fluxes.

The aim of this study is to determine sediment transport pathways between embayments on a high-energy coastline, providing order of magnitude estimates for potential bypassing rates between sediment compartments, across event to multi-annual timescales. Following the observational study conducted by Valiente et al. (2019b), variable local factors (wave exposure and sheltering, headland bypassing and embayment scale circulation) influencing the inter-annual sediment transport dynamics for 15 km of the macrotidal, exposed and embayed coastline of north Cornwall, SW England, are investigated using numerical simulations. A description of the study area is presented in Section 2. Section 3 describes the observational dataset used for calibration and validation purposes, model set up and selected modelled scenarios. Model results including major sediment pathways and fluxes are outlined in Section 4. Section 5.1 introduces the main mechanisms for redistributing material on the lower shoreface. Sediment exchange between the different embayments is reconstructed over multi-annual timescales and potential sediment budgets are provided in Section 5.2. Finally, conclusions are presented in Section 6.

2. Study area

The study encompasses a 15 km-long section of the macrotidal, exposed and embayed coastline of north Cornwall from Chapel Porth (Chapel) to Holywell (Holy) (Figure 1). This stretch of coast includes five sandy beaches delineated by sharp headlands of diverse morphometric characteristic (Figure 1e) that alternate with rocky sediment-free areas backed by cliffs 50 – 90 m high. The beaches are characterised by a wide low-gradient (mean bed slope ranging 0.018 – 0.021) sandy platform facing W with a slight rotation in the south to the NW (280° – 290°). The beaches are composed of medium sand with a median grain size (D_{50}) of 0.30 – 0.40 mm. St. Agnes (St. Ag) is the exception, facing N, with shorter length and coarser sand than the other embayments. For Perranporth (PPT), D_{50} attains a relatively constant value (0.33 mm) up to 20 – 26 m depth Ordnance Datum Newlyn (ODN; approximately -0.3 m MSL) (Valiente et al., 2019a), which is inferred as the base of the active profile. This coastline is considered cross-shore dominated with the onshore-offshore point of sediment transfer (i.e., the *pivot point* between erosion and accretion) between the upper shoreface and the shallow sub-tidal at 5 to 7 m depth relative to ODN (Valiente et al., 2019b). Isolated rocks are present around the apex of most of the headlands at depths of 5 – 10 m ODN. Sand is visible around these rocks in aerial imagery (McCarroll et al., 2018) and

smooth contours inferred to be sand are found off most of the studied headlands at depths between -17 and -26 m ODN (Valiente et al., 2019a). The averaged morphological depth of closure (*DoC*) along this stretch of coast determined from morphological observations is c. 15 m depth ODN (Valiente et al., 2019a), and the averaged maximum depth of transport computed using tide- and wave-induced bed shear stresses during extreme conditions is c. 25 – 28 m depth relative to ODN (Valiente et al., 2019a), consistent with the active profile depth determined from grain size.

This coastline is characterized by energetic waves from the W and WNW (Figure 1b) as a result of a combination of Atlantic swell and local wind waves. Annual average significant wave height (H_s) is 1.6 m and peak period (T_p) is 10 – 11 s (Figure 1c). A strong seasonality in the wave climate exists with monthly average H_s ranging from 1.2 m (summer) to 2.3 m (winter), and extreme wave heights can exceed H_s = 8 m and T_p = 19 s. The tidal regime is semi-diurnal and macrotidal with a mean spring and neap tidal range of 6.3 m and 2.7 m, respectively (Masselink et al., 2014; Scott et al., 2016). Maximum ebb and flood velocity ranges from 0.1 to 0.4 m s^{-1} at depths between 10 and 30 m with the tidal flows predominantly parallel to the shoreline, and with speeds significantly increasing around the headlands (c. 0.7 m s^{-1} during spring tides; Valiente et al., 2019a). The strong flood-ebb asymmetry in the current magnitude during a tidal cycle results in a northward residual current along the coast of 0.05 – 0.2 m s^{-1} (McCarroll et al., 2018).

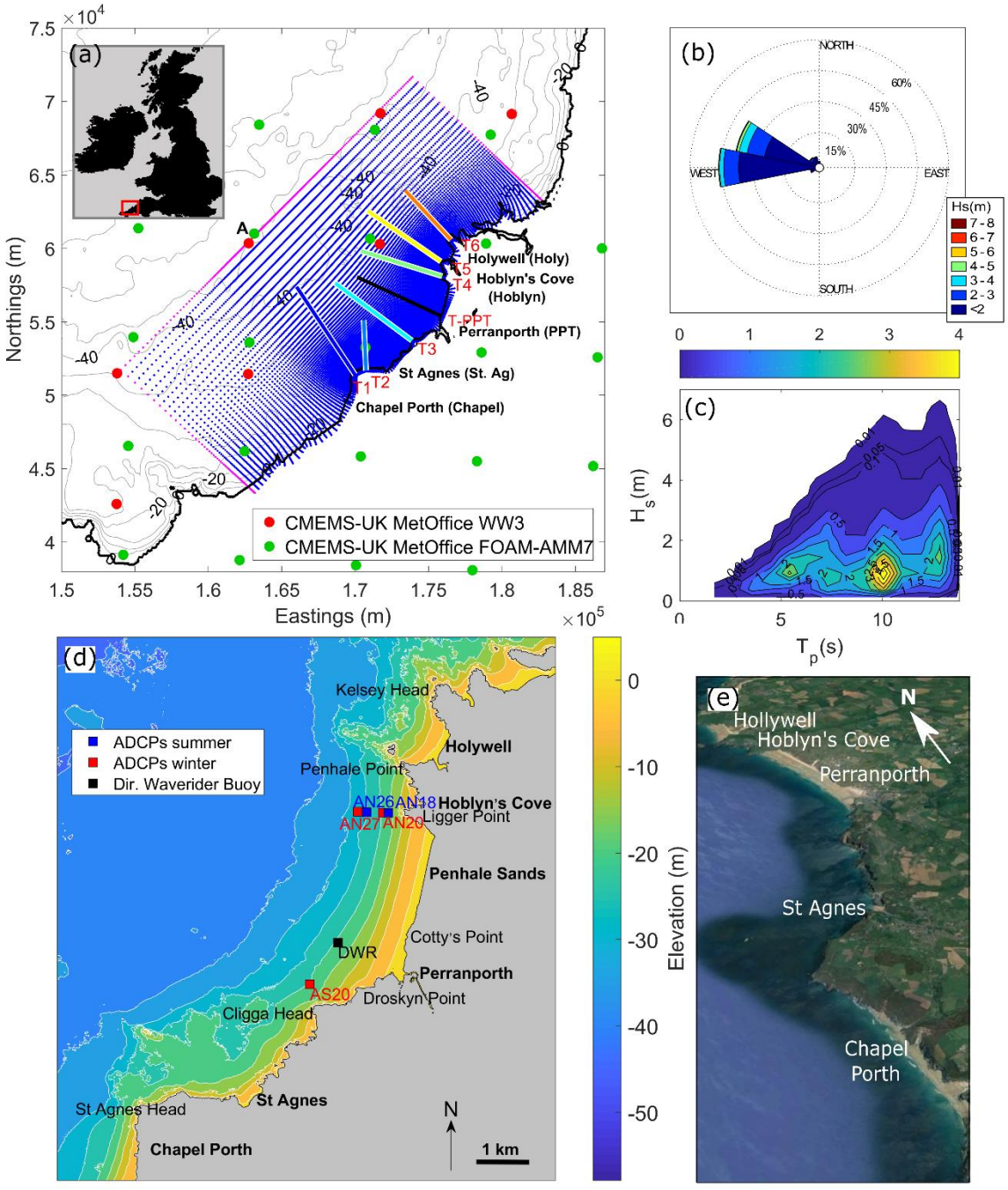

Figure 1. (a) Delft3D model grid and transects used for the analysis (thick solid lines). Red dots indicate UK MetOffice Wave Watch III 8 km (WW3) model nodes used as wave input and green dots represent Forecasting Ocean Assimilation Model Shelf Seas Atlantic Margin Model 7 km (FOAM-AMM7) hydrodynamic nodes provided by Copernicus Marine Environment Monitoring Service (CMEMS, 2017). Grid nodes are plotted every 2 points in each direction for clarity. Location **A** was used for examining boundary conditions for simulated sample cases. (b) Wave rose and (c) joint probability for Perranporth using 11 years of wave buoy data (DWR). (d) Physical context of the study site and instrument positions (squares). Instrument name refers to the location and mooring depth relative ODN, respectively, e.g., AS20 was the ADCP deployed in the south of the bay at 20 m water depth. (e) Oblique Google Earth image of headlands and embayments.

Timeseries of the monthly averaged temperature profiles and mixed layer depths obtained from the CMEMS North-West shelf reanalysis product (Tonani, 2019) indicate that the water column in this area can be considered generally fully mixed over the year. Data is extracted from the ocean physics reanalysis of the North-West European Shelf produced using the Met Office Forecasting Ocean Assimilation Model with a horizontal resolution of 7km (see O'Dea 2012, 2017 for the details). The reanalysis system assimilates satellite and in-situ Sea Surface Temperature (SST), and in situ temperature and salinity profiles (Tonani, 2019). The ocean mixed layer represents up to 90% – 100% of the total water column, with differences between surface and bottom temperature < 0.1ºC (Figure 2).

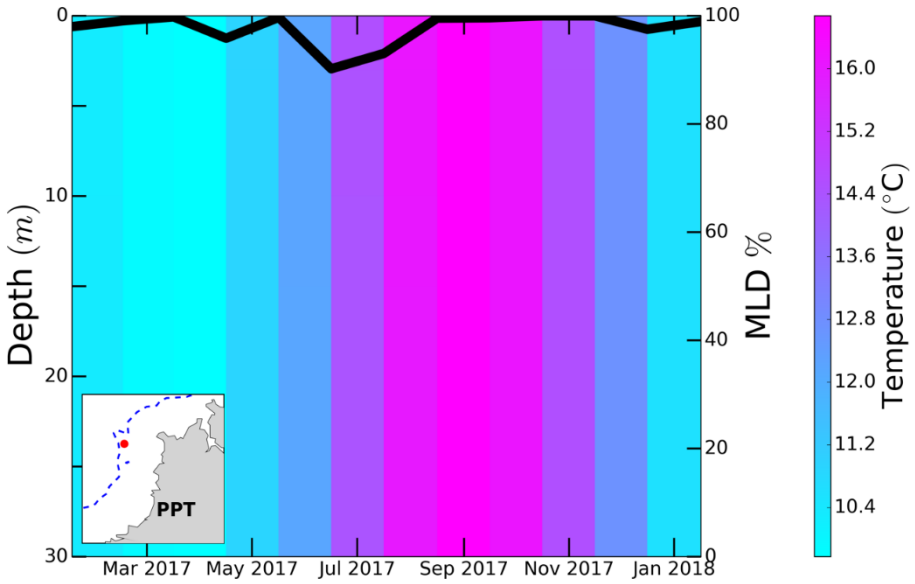

Figure 2. Time series of monthly average water column temperature and percentage of ocean mixed layer (MLD) at 40 m depth over 2017. The ocean mixed layer depth is defined by density as per Kara et al. (2000). Data corresponds to the ocean physics reanalysis for the North-West European Shelf (CMEMS, 2017) produced using an ocean assimilation model (NEMO; Madec et al., 2016) and a modified version of NEMOVar data assimilation code (Mogensen et al., 2012). The reanalysis system assimilates satellite and in-situ Sea Surface Temperature (SST) and in situ temperature and salinity profiles (Tonani, 2019). Zoomed-in location of the ocean reanalysis node is shown in the inset.

3. Materials and Methods

3.1 Waves, water levels and current observations

Waves, currents and water levels were measured using three 600 kHz RDI WorkHorse Monitor Acoustic Doppler Current Profilers (ADCPs) deployed for 2 – 3 months in summer 2016 (AN17 and AN25) and winter 2016/17 (AS20, AN20 and AN27) off the two headlands delineating Perranporth beach in 15 – 30 m depth relative to ODN (Figure 1d). Two ADCPs

located shore-normal to the apex of the northern headland (same transect, 475 m apart) were moored during summer and winter periods with an extra ADCP located perpendicular to the southern headland during winter. Waves were also observed by a directional wave buoy (DWR, Figure 1d) located in 20 m depth that recorded every 30-min. Currents were ensemble averaged at 5-min intervals using 90 pings per averaged ensemble per current profile at 0.33 Hz (over 270 s). The waves measured by the ADCPs were recorded every 2 h using 20-min bursts at 2 Hz (2400 samples). Current observations were post-processed and cleaned prior to sample averaging to avoid overestimation due to frequent spikes. Surface spikes were removed applying the Return Signal Strength Indicator (RSSI) for spike detection, which conducts a cut-off in the velocity profile where the threshold in the RSSI is exceeded. Remaining spikes were cleaned using the phase-space thresholding method by Goring and Nikora (2003). The time series was then reconstructed using a cubic polynomial. Wave and current observations were used to calibrate and validate the numerical model Delft3D. The currents were vertically-averaged using all bins over the water column and smoothed using a 30-min moving average filter. A comparison between averaged modelled currents and observed bottom bin currents revealed minimum differences between the two (< 0.05 m s^{-1}). Hence, the use of depth-averaged currents was considered appropriate for validation purposes.

3.2 Numerical model setup

The process-based numerical model Delft3D (Roelvink and van Banning (1994); Booij et al., 1999) was used for wave transformation (WAVE), and computation of wave and tide induced flows (FLOW). The FLOW module solves the 3D water equations and the WAVE module includes the wave propagation, dissipation, generation by wind and non-linear wave-wave interactions. Delft3D was run in 2D (i.e. depth averaged) and online-coupled mode (i.e. two-way wave-current interaction).

3.2.1 Model forcing datasets

Time series of waves, vertically averaged currents and water level were used as model forcing. Hourly bulk parameters of wave characteristics (H_s, T_p, *Dir*, and directional spread) from the UK MetOffice Wave Watch III 8 km (WW3) model nodes were linearly interpolated at intervals to the WAVE model boundaries. Hourly water level and current time series (vertically-averaged) were extracted from the Forecasting Ocean Assimilation Model Shelf Seas Atlantic Margin Model 7 km (FOAM-AMM7). Equally to the wave forcing, current and

water level forcing conditions were linearly interpolated to the boundaries of the FLOW model. Both wave and hydrodynamic model datasets were generated by UK MetOffice and provided by Copernicus Marine Environment Monitoring Service (CMEMS, 2017).

Atmospheric pressure forcing conditions (6-hourly) were obtained from the National Oceanic and Atmospheric Administration (NOAA) Climate Forecast System Version 2 (CFSv2) at 0.5° resolution. 6-hourly wind forcing data was obtained from the L4 dataset CERSAT Global ocean blended wind dataset at 0.25° resolution produced by IFREMER and distributed by the CMEMS Ocean and Sea Ice Thematic Assembly Centre (OSI TAC). Wind and pressure forcing data were linearly interpolated and presented in a spatially-varying separate grid.

3.2.2 Bathymetry and model domain

The high-resolution initial bathymetry was created by combining a multimethod morphological dataset for the year 2011. This bathymetry was constructed by merging Light Detection And Ranging (LiDAR), RTK-GPS aided single-beam survey and multi-beam bathymetry provided by the United Kingdom Hydrographic Office. A 2-m spatial resolution digital elevation model (*DEM*) was generated for the entire stretch of coast using Loess (Plant et al., 2002) and natural neighbor (Sibson, 1981) interpolation functions. The DEM was referenced to ODN and corrected to MSL. Due to the resolution of the hydrodynamic forcing conditions (7 km), a transition zone with a smoother bathymetry was implemented to eliminate an inaccurate strong coastal current induced at the cross-shore boundaries. Additionally, a 2-D Gaussian smoothing filter with standard deviation of 2 was exclusively applied along 400 m extent at lateral (alongshore) ends of the domain. The model domain was large enough to maintain the transition zones far from the area of study.

The model domain encompasses Perranporth beach and adjacent embayments using two orthogonal curvilinear grids (Figure 1a) generated using conformal mapping methods as in Bruciaferri et al. (2019) with an extent of 15 km by 10 km and a space-varying resolution that ranges from 300 m offshore to < 20 m near the coast. These grids are designed to follow the primary morphological features along the study coastline such as headlands and bays, while being able to resolve the coastline with higher resolution. The WAVE grid has a 2-grid cell (0.36 km) halo at the boundaries of the FLOW grid. Sensitivity analysis of this final setup was performed against a WAVE grid with a halo extension of c. 4.5 km (25-grid cells) at each

boundary (not shown) and simulations showed equal performance of the two implementations, discarding the necessity to extend the wave domain more than 2-grid cells.

3.2.3 Wave model

The third-generation spectral wave model SWAN (Booij et al., 1999), packaged within Delft3D as WAVE, was used to transform wave conditions from offshore to inshore. This model accounts for wind growth, dissipation processes and wave-wave interactions. The dissipation mechanisms considered were bottom friction (with JONSWAP friction coefficient of 0.067 m^2 s^{-2}), refraction, whitecapping (Komen et al., 1984) and depth-induced breaking (with ratio of maximum individual wave height over depth equal to 0.7; Luijendijk et al., 2017). Non-linear wave-wave interactions were also considered. Bulk parameters of wave characteristics (H_s, T_p, *Dir*, and directional spread) from UK MetOffice Wave Watch III 8 km (WW3) were used as forcing conditions and WAVE was run in stationary mode.

3.2.4 Flow model

Flow and sediment transport computations were conducted using the FLOW module. The FLOW model was implemented in 2DH, solving the depth-averaged shallow water equations, and run in hydrostatic mode. Previous coastal studies of similar spatial scale on energetic sandy coastlines (e.g., Luijendijk et al., 2017) have demonstrated that Delf3D run in 2D mode is able to accurately reproduce hydrodynamic behaviour over multi-annual timescales. Other modelling approaches encompassing larger areas of this coast have also shown good replicability of observed hydrodynamic processes (Holt et al., 2001; Bricheno et al., 2015; Lyddon et al., 2018). Additionally, King et al. (2019) studied major sand transport pathways on the SW continental shelf, demonstrating that qualitatively the spatial pattern of net sand transport remained the same after the addition of multiple sigma levels (vertical layers based on a proportion of the depth), i.e., after implementing a 3D model. Consequently, depth-averaged hydrodynamics were considered adequate for this study as sediment fluxes to larger depths will be almost entirely driven by the relatively depth-uniform rip cell circulation that the model in 2D mode is able to reproduce. More details on model design rationale and limitations are presented in Section 3.2.5.

Several methods for open boundary conditions can be implemented for nested modelling on Delft3D. Although traditionally it is recommended to use different boundary conditions for coastal models (Deltares, 2014), it is well known that undesired boundary effects can still remain (Qinghua Ye et al., 2011). After several sensitivity analyses using Neumann and water

level as cross-shore boundary conditions, the optimal forcing configuration was determined as water level time series at two open boundaries (offshore NW and cross-shore NE) and current time series at the inflow open boundary (cross-shore SW). Additionally, several test cases with a range of boundary reflection parameter *Alfa* values (10 – 200) were set up to assess the best performance. *Alfa* specifies the amount by which the open boundary is less reflective for short wave disturbances that propagate towards the boundary from inside the model and for macro-tidal environments is recommended a value of 50 or 100 (Deltares manual, page 46). A final *Alfa* value of 50 showed the best performance.

Following Luijendijk et al. (2017), bed-load and suspended-load (both current- and wave-related) sand transport rates were computed using the TRANSPOR2004 transport formulation (van Rijn, 2007a, 2007b) with uniform sediment size of 0.33 mm (Prodger et al., 2017) and unlimited sediment availability on areas defined by the sdb file. The FLOW model was run using a 0.05-min time-step to avoid large Courant number values during the simulated periods with extreme wave conditions. The MORPHO module was turned on with update off and transport model settings employed in the model runs were extracted from similar studies (Table 1).

Table 1. Delft3D model settings.

Module	Parameter	Value/Setting	Comment
Hydrodynamics	Boundaries	cross-shore SW – current Offshore – WL cross-shore NE – WL	Different combinations for the cross-shore boundaries (e.g., Neumann) were tested.
	Reflection	50	Test from 10 to 200.
Transport	Formulation	Van Rijn (2007b)	'TRANSPOOR2004', as per Luijendijk et al. (2017).
	D50	0.33 mm	As per Prodger et al. (2016)
	Transport multipliers	Sus (1.4), Bed (0.8), SusW (0.3), BedW (0.3)	Suspended and bed transport multipliers for currents (Sus, Bed) and waves (SusW, BedW). As per Grunnet et al. (2004).
Morphology	Update	Off	-
	CaMax	0.05	Limiters to avoid unrealistic suspended sediment transport fluxes. As per Elias (2018).
	DzMax	0.05	

3.2.5 Model limitations

Delft3D has been successfully used in a depth-averaged form in studies of wave-current interactions and sediment transport on the inner continental shelf (Hansen et al., 2013; Hopkins et al., 2015; Ridderinkhof et al., 2016; Luijendijk et al., 2017; King et al., 2019). The influence

of water column stratification in the circulation pathways of the study area can be considered minor as vertically mixed conditions are being maintained all year (refer to Figure 2; e.g., Sharples et al., 2013). Additionally, this stretch of coastline does not include any estuary nor any important effluent that may cause stratification of the water column.

Processes such offshore (bed return flow) and onshore (wave asymmetry) cross-shore fluxes are poorly resolved in a depth-averaged model, limiting cross-shore sediment transport to the relatively depth-uniform rip circulation driven by longshore morphological variations in the bathymetry (Bakhtyar et al., 2016). However, it is emphasized that the main focus of this research is on the sediment transport along the lower shoreface, in which Delft3D in 2D-mode has been shown to be effective (Hsu et al., 2006; Luijendijk et al., 2017) and comparable to a 3D model (Huisman et al., 2018; King et al., 2019). Parameters such SUSW (suspended transport due to waves) can be tuned to avoid overestimation of cross-shore fluxes in 2DH (e.g., Van Rijn et al., 2004; Giardino et al., 2011) and in this study the SUSW parameter was therefore set to 30% (Table 1) as per Luijendijk et al. (2017). In order to assess model limitations and assumptions, an additional 3D test using 10 sigma levels was run only for the first week of January 2014. The 3D test followed the same setup as the 2DH test.

Other model assumptions include uniform sediment size (averaged D_{50} = 0.3 mm) and unlimited sediment supply; thus, resulting sediment budgets must be considered exploratory in nature as the predicted rates of sediment fluxes disregard areas of different sediment size and periods with sediment deficit. It is also noted that the use of different sediment transport formulations can provide very different results and, as actual sediment fluxes measurement were lacking, the widely applied sediment transport formulation *TRANSPOOR2004* (Van Rijn; 2007b) was used here.

3.2.6 Model calibration and validation

Model output was calibrated against four points of observations of wave statistics (DWR, AS20, AN20 and AN27), and three of water level and flow velocity and direction (AS20, AN20 and AN27) for March 2017 (refer to Figure 1d for locations). The model performance was then optimised for the calibration period and then validated against a total of two months observations covering a wide range of summer and winter wave hydrodynamic conditions. Summer and winter validation periods were August 2016 and February 2017, respectively. Model skill was evaluated using root-mean square error (*RMSE*), mean absolute error (*MAE*), *bias* and coefficient of determination (R^2). *Bias* was normalised relative to the observed

mean, so that the systematic error of the model was expressed in terms of the background observed sample climate.

3.3. Modelled scenarios

Computational requirements for a 8-year period (2011 – 2018) are excessive; therefore, we opted for shorter model runs (Figure 3a-dashed boxes) covering a wide range of representative wave conditions, namely H_s = 0.1 – 8 m, T_p = 4 – 20 s and *Dir* = 260 – 360º (Figure 3e) over different tidal ranges (neap to spring tides, Figure 3f). Frequency distributions of the wave statistics and water-level conditions for the selected model simulations are shown in Figure 3b–d. To facilitate visual comparison with the complete hindcast model forcing time series encompassing 2011 – 2018, the simulated cases are presented using a fitted distribution. Representativeness of the selected periods is demonstrated as all variables follow the distribution of the complete time series (Figure 3b–d). Model simulations were performed over a total of 6 months: (i) a 2-month period over a characteristic summer (2016); (ii) a c. 3-month period over winter (2016/17), with both periods also used for validation; and (iii) an extra 1-month of exceptional extreme energy conditions, January 2014 (H_s ~ 8 m; Masselink et al., 2016a,b).

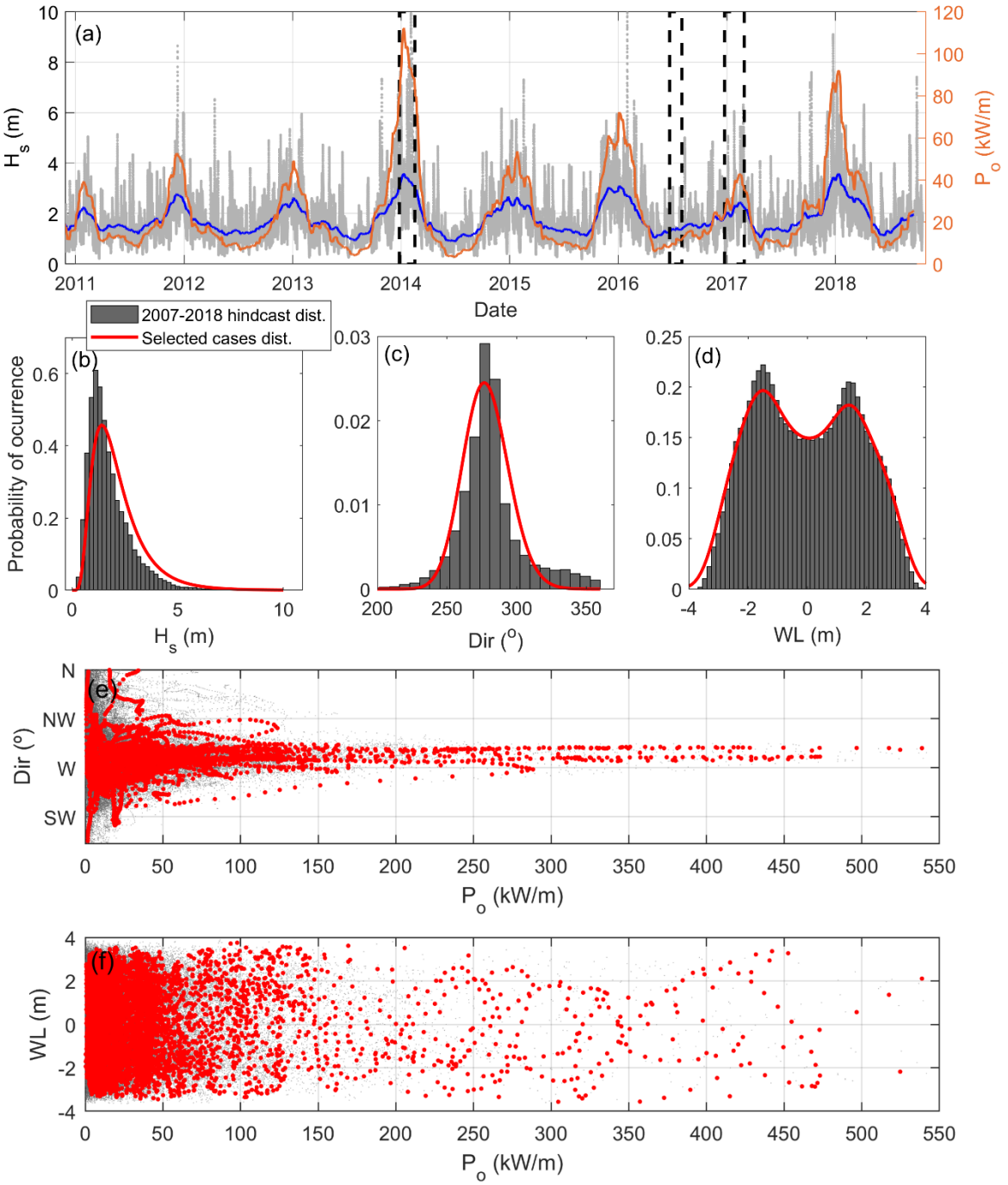

Figure 3. (a) 8-year time series of significant wave height *Hs* (30-min and 4-week running mean) and wave power *Po* (Herbich, 2000). Normalised probability of occurrence for H_s (b), wave direction *Dir* (c) and water level *WL* (d) based on the complete hindcast from 2011 – 2018, compared to distribution of the selected cases for model runs (dashed boxes in a). (e, f) Distribution of selected cases for the combinations of P_o, wave direction (*Dir*) and water level (*WL*). Red and grey dots represent selected cases and total hindcast, respectively. All variables correspond to the CMEMS nodes located at the centre of the offshore boundary of the model domain (Location A, Figure 1a).

3.4 Transects for transport fluxes integration

Six transects (refer to Figure 1a) extending from the headland apex to > 35 m ODN were used to compute sediment transport rates between bays. Transects were located at the primary headlands and drawn perpendicular to the headland apex. Sediment fluxes (sum of bed-load and suspended-load) were integrated over each transect (Q_{bypass}) for different range of depths: < 6 m, 6 – 15 m, 15 – 25 m and > 25 m water depth ODN. Alongshore sediment fluxes were also computed across one extra profile located on the middle of Perranporth beach. Longshore drift direction was calculated with respect to the transect orientation in order to discern between inflows and outflows in/out of the different embayments, with positive (negative) values indicating northward (southward) flux.

4 Results

4.1 Calibration and validation

WAVE output over the validation period is compared with observations in Figure 4. Visual inspection indicates that the model correctly reproduced the experienced wave conditions. The model satisfactorily replicated wave height (averaged model skill values for all locations were *RMSE* = 0.40 m, *MAE* = 0.29 m, R^2 = 0.79 and *bias* = 0.05; Table 2) for both summer and winter validation periods. The peak period prediction was good (average model validation coefficients for all locations were *RMSE* = 2.1 s, *MAE* = 1.3 s, R^2 = 0.65 and *bias* = 0.01; Table 2), with poorer correlations during short periods (T_p < 10 s; Figure 4) when wave period was overestimated. Modelled wave direction oscillated around the prevailing direction (~280°) and showed little long-term variation (maximum *bias = 0.12*), therefore R^2 showed poor correlations and is not the best indicator of model performance. *RMSE* and *MAE* are better indicators in this instance with values for wave direction oscillating between 9 – 17° and 9 – 11°, respectively; values comparable to those found in similar studies (Vieira da Silva et al., 2016; McCarroll et al., 2018).

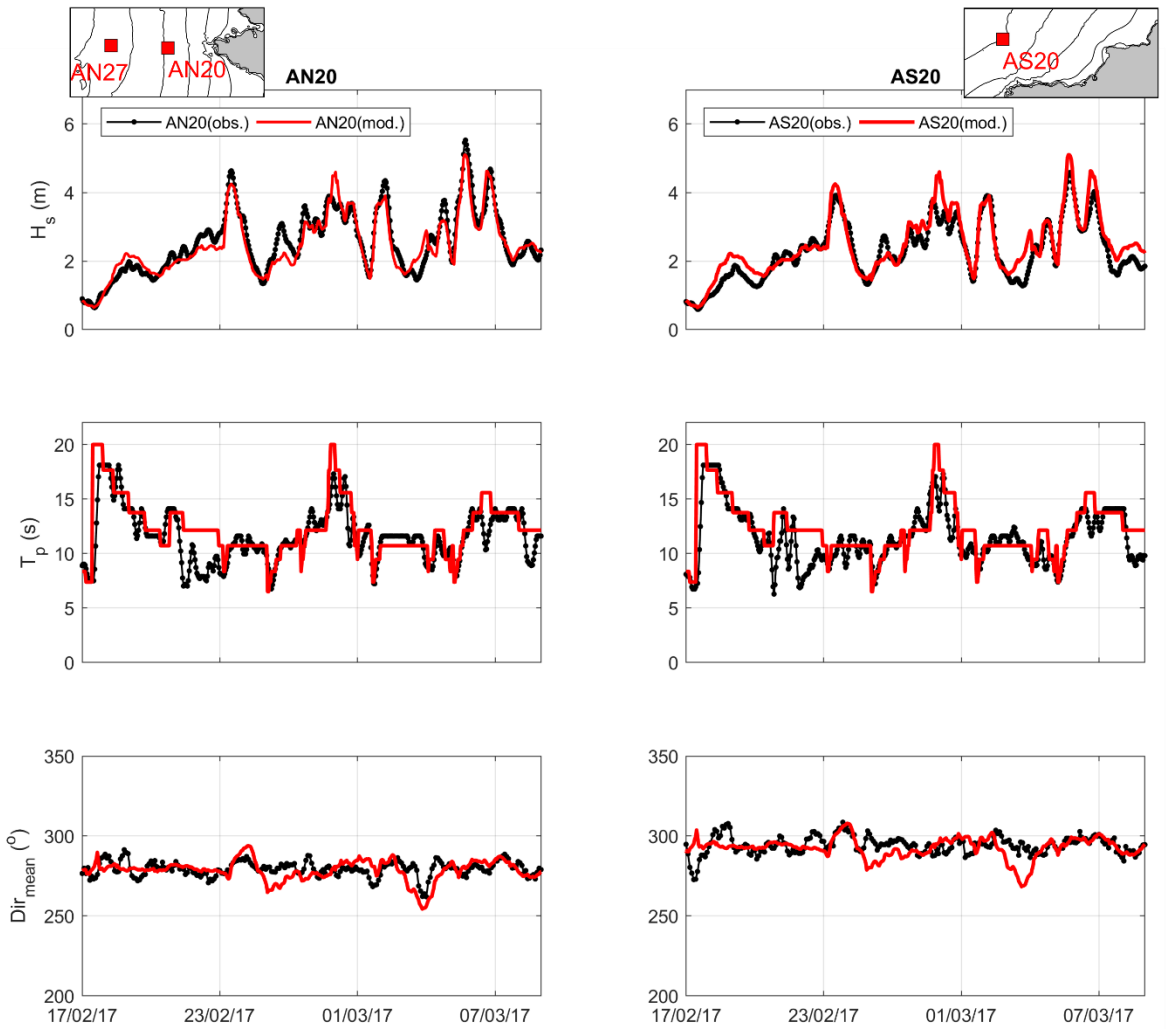

Figure 4. Wave ADCP observations at AN20 and AS20 compared with Delft3D model output. From top to bottom: significant wave height (*Hs*), peak period (*Tp*), and mean direction (Dir_{mean}). Zoomed-in locations of the ADCPs are presented in the small top panels; cf. Figure 1d for large-scale setting of the ADCP locations.

Observed and modelled FLOW output over a month of simulations encompassing two neap and two spring periods are presented in Figure 5 and 6. Overall, water level and flow simulations reproduced the observations well. For the northward headland (AN20 and AN27), a residual current of 0.05 and 0.25 m s^{-1} (*U*; Figure 5d,h) was observed during neap and spring tides, respectively. The flow was mainly explained by the alongshore component (*v*, northward current) (Figure 5b,f), with minimal cross-shore flows (*u*, eastward current) (Figure 5c,g). Conversely, AS20 deployed off the southern headland showed a velocity signal that is explained c. 60% by the cross-shore component (-0.4 – 0.5 m s^{-1}, Figure 6d) and, although the model is able to reproduce the cross-shore signal qualitatively (refer to Figure 6a), the cross-shore flow is underestimated during neap tides and overestimated during spring tides (Figure 6d).

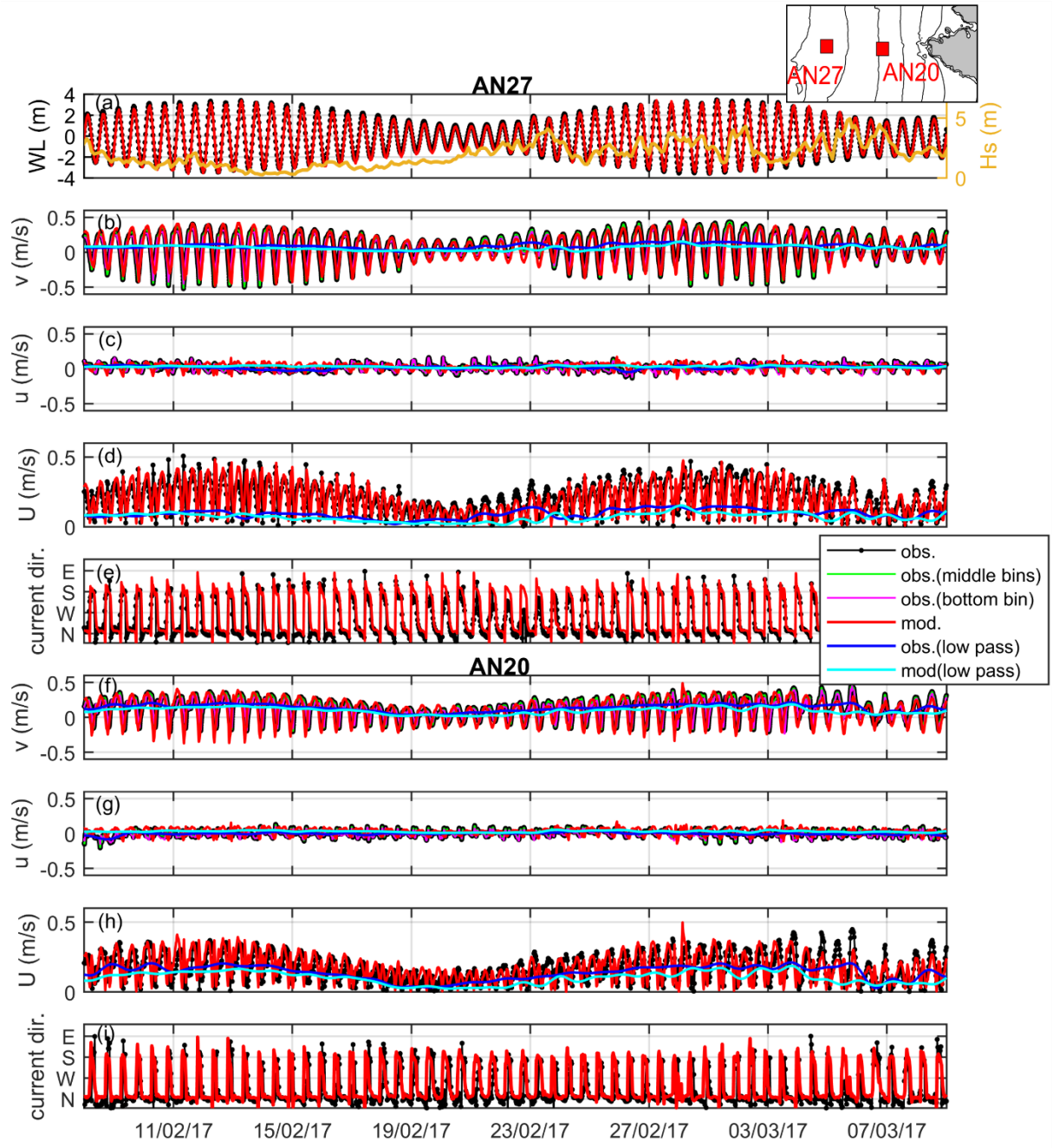

Figure 5. (a) Water level (*WL*) and flow observations at ADCPs AN27 (a – e) and AN20 (f – i) compared with Delft3D model output over February 2017. Flow observations include: (b, f) northward current component (*v*), (c, g) eastward current component (*u*), (d, h) flow speed (*U*) and (e, i) direction (current dir.). Flow variables are 30-min averages whereas WL is 2-hourly. Flow observations include average currents using all bins (obs.), average currents over the middle bins (obs. – middle bins) and bottom currents (obs. – bottom bin). Low-pass flow speed has a 25-h cut-off Fourier transform filter applied. For reference, observed significant wave height at AN27 (orange line in top panel) is presented. Zoomed-in locations of the ADCPs are shown in the small top panel; cf. Figure 1d for large-scale setting of the ADCP locations.

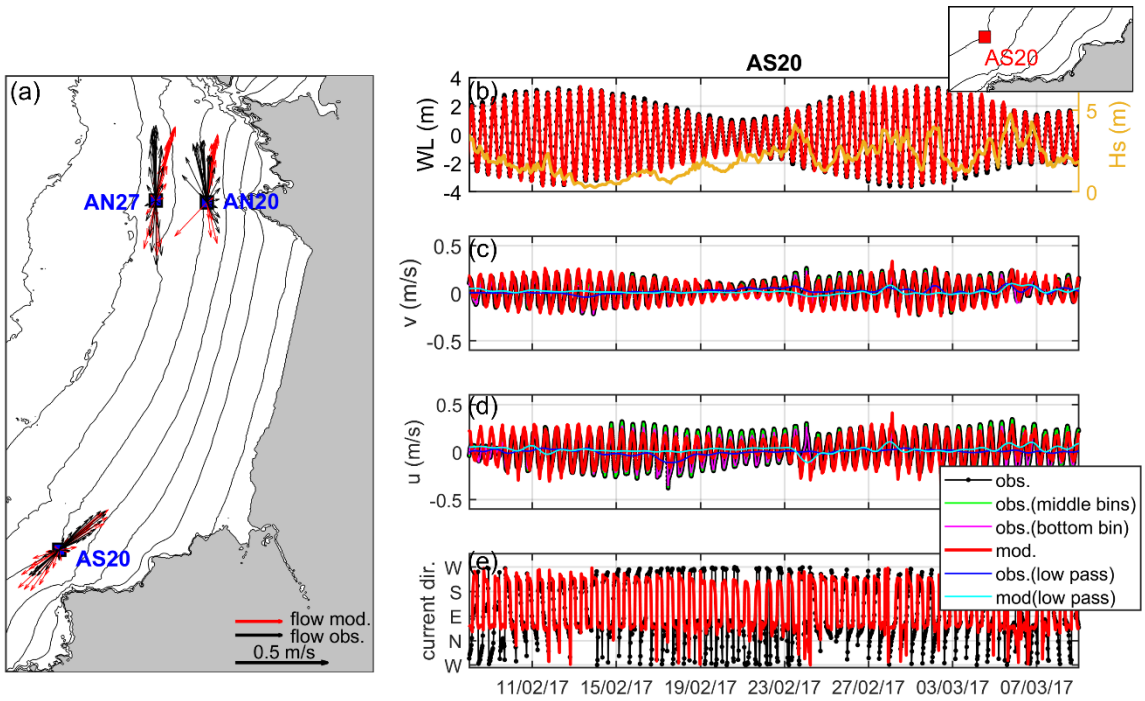

Figure 6. (a) Flow based on observations (black) and model output (red) for a representative tidal cycle at the ADCPs locations. Observations compared with Delf3D model output over February 2017 for (b) water level (*WL*), (c) northward current component (*u*), (d) eastward current component (*v*), and (e) direction at ADCP AS20. Flow variables are 30-min averages whereas *WL* is 2-hourly. Flow observations include average currents using all bins (obs.), average currents over the middle bins (obs. – middle bins) and bottom currents (obs. – bottom bin). Low-pass flow speed has a 25-h cut-off Fourier transform filter applied. For reference, observed significant wave height at AS20 (orange line in right top panel) is presented. Zoomed-in location of the ADCP is shown in the small top panel; cf. Figure 1d for large-scale setting of the ADCP location.

Water level prediction was excellent (averaged *RMSE* = 0.20 m, averaged *MAE* = 0.11 m, averaged R^2 = 0.97 and averaged *bias* = 0.02; Table 2), and current velocity and direction were accurately modelled for the northern ADCPs (averaged *RMSE* = 0.07 m s^{-1} and 51°; averaged R^2 = 0.5 and 0.66, respectively; Table 2). The large *RMSE* value for direction is related to a time offset in the tidal directional change, such that for short periods the direction is off by ~180°. Skill values showed a better model performance reproducing currents where the flow was primarily alongshore with minimal cross-shore currents (instruments perpendicular to the northern headland; AN18, AN20, AN26 and AN27). Consequently, velocity magnitude at the AS20 location, where the cross-shore signal was under- or overpredicted, was not well reproduced by the model but this should not represent major differences when computing fluxes between the different bays as the longshore component is well reproduced. The flow at AS20 presented *RMSE* values similar to the rest of validation points (*RMSE* = 0.09 and *MAE*

= 0.07 m s^{-1}; Table 2), but it showed weak correlation (R^2 = 0.34; Table 2). Overall, the model performance is considered good at predicting wave and hydrodynamic conditions.

Table 2. Model validation coefficients.

	Model	Variable	Location	*RMSE*	*MAE*	R^2	*Bias*
Summer 2016	WAVE	Significant wave height (m)	AN26	0.32	0.25	0.76	0.03
			AN18	0.31	0.24	0.76	<0.01
			Buoy	0.32	0.24	0.77	<0.01
		Peak period (s)	AN26	1.5	0.95	0.50	0.01
			AN18	1.44	0.94	0.53	0.01
			Buoy	1.62	1.05	0.51	0.02
		Mean direction (deg.)	AN26	9.12	8.55	0.09	0.12
			AN18	11.73	9.05	0.03	<-0.01
	FLOW	Water level (m)	AN26	0.25	0.15	0.97	0.01
			AN18	0.24	0.16	0.97	0.01
		Flow speed (m/s)	AN26	0.06	0.04	0.59	<0.01
			AN18	0.05	0.04	0.58	<0.01
		Flow direction (deg.)	AN26	41	25.84	0.77	0.38
			AN18	44	27.52	0.70	0.4
Winter 2017	WAVE	Significant wave height (m)	AN27	0.48	0.36	0.7	0.04
			AN20	0.46	0.34	0.81	0.05
			AS20	0.48	0.36	0.74	0.09
			Buoy	0.47	0.35	0.81	0.09
		Peak period (s)	AN27	2.83	2.03	0.27	0.01
			AN20	2.12	1.43	0.51	0.01
			AS20	2.22	1.49	0.50	0.02
			Buoy	2.01	1.34	0.58	0.02
		Mean direction (deg.)	AN27	17.13	11.84	0.44	<0.01
			AN20	10.91	8.04	0.76	<0.01
			AS20	17.31	11.93	0.76	<0.01
	FLOW	Water level (m)	AN27	0.16	0.11	0.97	0.04
			AN20	0.13	0.09	0.97	<0.01
			AS20	0.13	0.09	0.98	<0.01
		Flow speed (m/s)	AN27	0.07	0.05	0.59	<0.01
			AN20	0.09	0.07	0.52	<0.01
			AS20	0.09	0.07	0.34	0.04
		Flow direction (deg.)	AN27	48.49	34.84	0.63	0.39
			AN20	69.00	52.54	0.66	0.35
			AS20	73.53	61.8	0.44	0.82

An additional comparative test using a 3D model setup was run over 1-week of January 2014. Bed shear stress and total sediment transport including both suspended and bedload fluxes were computed over conditions of maximum stress when differences between a 2DH and a 3D model approach are expected to be greater. Results showed that both models produced a bed shear stress distribution (Figure 7a,b) with: (i) the largest shear stress (> 7 N m^{-2}, northward) along a confined narrow band at the coast (landward of 20 m depth); and (ii) a significant bed shear stress decay (< 0.75 N m^{-2}) beyond the 25 – 30 m isobaths. The addition of sigma layers enhances the bed shear stress with a larger relative increase offshore within a factor of two. These differences are likely to be related with the lack of representation of some effects of wave-current interaction and the parameterization of turbulence due to wave breaking and bottom friction in 2DH mode (King et al., 2019). Despite these discrepancies, total sediment fluxes predicted by both models were of the same order (c. 10^{-4} m^3 s^{-1} m^{-1}) and followed the same pattern (Figure 7c,d). A fully 3D approach may produce differences in flux rates within a factor of two, which for our purposes is considered insignificant, as we are exploring order of magnitude scale response. Thus, the use of a depth-averaged model was considered appropriate for this particular study.

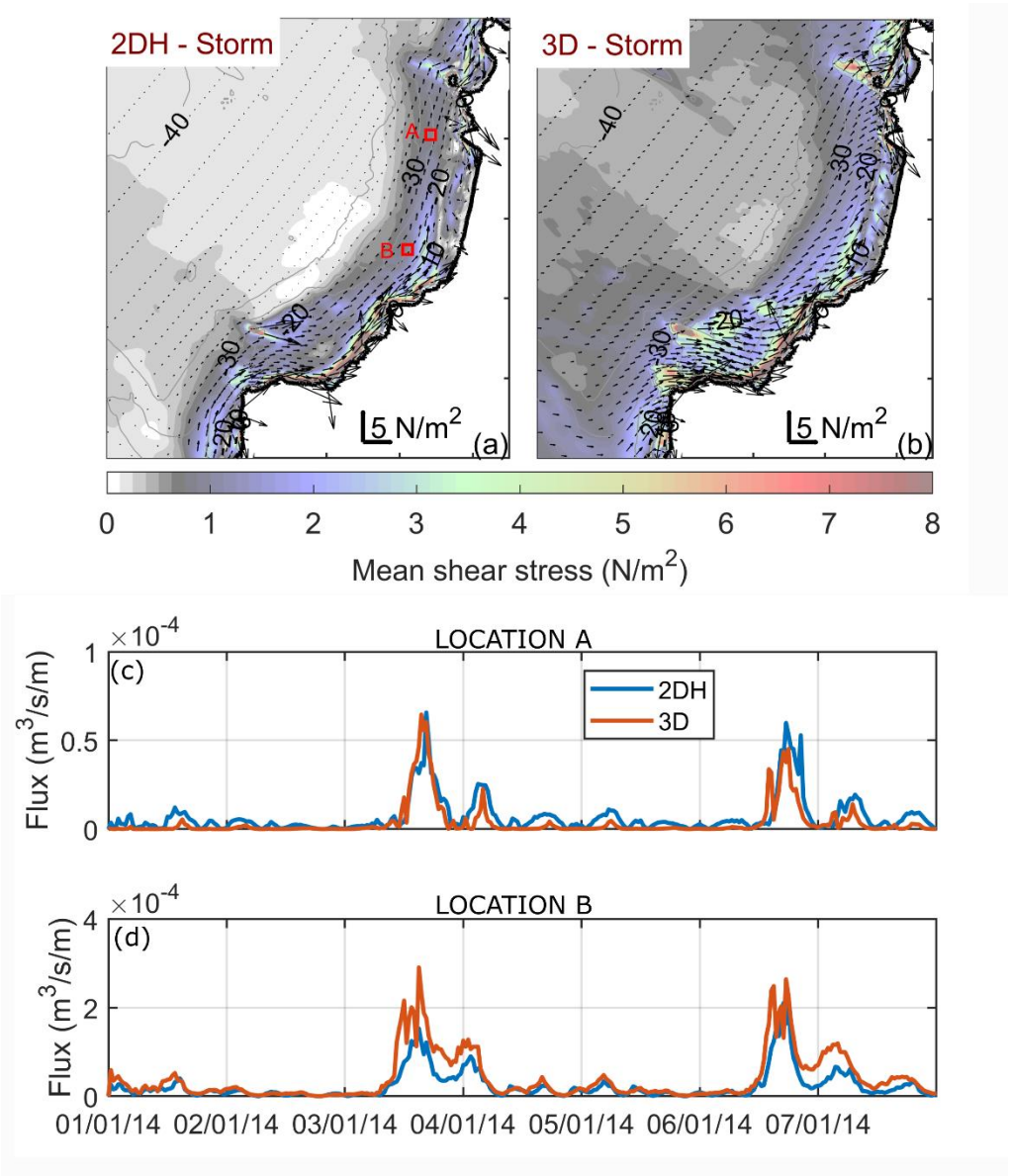

Figure 7. Bed shear stress and time series of total fluxes computed using a 2DH and a 3D model during high energy conditions. (a, b) Bed shear stresses are time-averaged over 12.5 h of storm Hercules, 2013/14 winter. (c, d) Time series of total fluxes include both suspended and bedload sediment transport. For reference, locations A and B for time series of sediment fluxes are included in (a).

4.2 Numerically modelled circulation

Simulations of coupled wave-driven and tidal currents (tide-averaged) are presented in Figure 8 to aid in the interpretation of sediment flux pathways over three embayment-scale circulation modes: moderate-high waves from the W; moderate-high waves from WNW; and extreme waves from W – WNW. The major components of circulation along this coastline include: (i) dominant northward residual tidal current in the vicinity of most of the headlands, (ii) northward current in the offshore region (> 15 m), and (iii) southward current in the shallow

nearshore (< 15 m) within the embayment as a result of the (iv) embayment-scale circulation. For shorter embayments, the clockwise circulation is cellular (strong headland control, one circulation cell fills the embayment), while for longer embayments, the circulation is intermediate (moderate headland control, several rip cells may be present along the embayment; Short and Masselink, 1999). For moderate-high wave forcing (H_s ~ 4 m) from the W (*Dir* ~ 270°; Figure 9a, d), clockwise embayment-scale circulation dominates in all the embayments (except St. Agnes). A narrow and strong northward (1 m s^{-1}) current is generated by oblique wave breaking near the headlands. The northward current is diverted offshore in the south of the long embayments (i.e., Perranporth and Chapel Porth) by a southward flow associated with the up-wave headlands at the north. This rip cell circulation is observed in all the embayments except St. Agnes, where the northward flow is deflected offshore (0.4 m s^{-1} up to 30 m depth) but does not recirculate. A headland rip at the north of Perranporth (up-wave headland) and large headland rips (mega-rip) at the down-wave headlands at the small embayments resulting from the cellular circulation are also evident for moderate to high-energy wave conditions.

For moderate-high wave forcing (H_s ~ 4 m) from the WNW (*Dir* ~ 286°; Figure 8b, e), the embayment-scale circulation pattern is still observed, but now a southward flow up to -10 m ODN within the embayment is present. The northward current in the offshore region is very weak (~ 0.1 m s^{-1}) and is only observed beyond the 15 m depth ODN. Headland rips that reach a maximum depth of 12 – 15 m and of smaller magnitude (< 0.4 m s^{-1}) than those for events from the W are only observed in the short bays (e.g., north of St. Agnes, Hoblyn's Cove and Holywell). It is noteworthy that for only a modest change in wave direction from 270° to 286°, the direction of the nearshore currents along this embayed coast changes considerably.

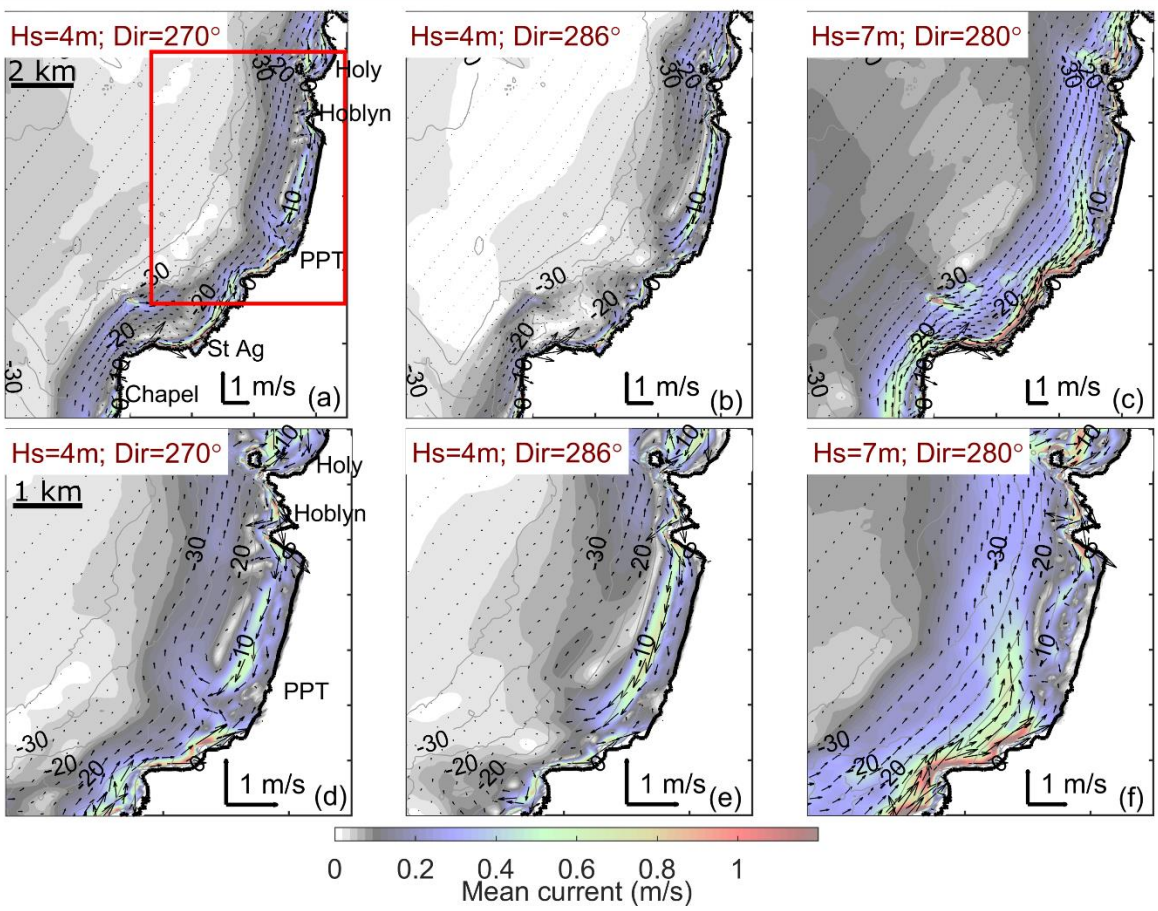

Figure 8. Time-averaged (12.5 h) currents (top panels) with zoom focused on Perranporth embayment (bottom panels) under storm conditions during spring tides. Circulation under moderate-high waves from the W (a, d), WNW (b, e) and extreme waves during storm Hercules, 2013/14 winter (c, f). *Hs* and *Dir* presented for each scenario correspond with offshore conditions at location A, refer to Figure 1a. For reference, embayment names abbreviations and bottom panels inset area (red box) are included in first column panels.

A strong (> 1 m s^{-1}) northward current along the coast and a surf zone extending beyond most of the headland apexes (> 0.4 m s^{-1} at 30 m depth) is predicted for extreme wave forcing (H_s ~ 7 m) from the W to WNW (Dir ~ 280°; Figure 8c, f). Consequently, the major circulation pattern can encompass several embayments for shallower bounding headlands, with a subsequent flow shift from the prevailing north direction towards the south close to the base of these (e.g., southward bypass between Hoblyn and Perranporth). During this circulation mode, the northward current is now deflected further offshore (c. 1 km long) at the longer embayments, Chapel Porth and Perranporth. This offshore-directed current of 0.7 m s^{-1} reaches up to -20 m ODN in the southern sector of the embayment. A headland rip is only observed in Hoblyn's Cove, but this is distorted by the strong northward current that exceeds 1.2 m s^{-1} in the stretches of coast highly oblique to wave direction such as the sector from St. Agnes Head to Droskyn Point.

4.3 Numerically modelled sediment fluxes

4.3.1 Gross sediment transport

The gross longshore transport (LST_{gross}) is computed as the total transport up (northward) and down (southward) the coast over the six month simulation (t = 6 months; January 2014, July – Aug 2016 and January – March 2017; Figure 9). LST_{gross} is integrated over the shoreface using the six transects perpendicular to the headlands and one transect located in the center of Perranporth bay (T-PPT) representative of an "open beach" (length of Perranporth beach is > 3.5 km). Results show that the largest rates of sediment transport occur between the headland apex and the 20 m contour line, and these fluxes decay significantly beyond the 25 m contour line. Additionally, it is evident that the largest LST_{gross} values occur around Perranporth beach (T3, T-PPT, T4), and these are 1 to 2 orders of magnitude larger than the gross bypass around the other headlands. Examining Perranporth transects individually, peaks of LST_{gross} are at 8 m (1250 $m^3\ m^{-1}$ for T3 and 680 $m^3\ m^{-1}$ for T4) and 5 m (600 $m^3\ m^{-1}$ for T-PPT) depth relative to ODN for the headlands (T3 and T4; Figure 9d,f) and the center of the beach (Figure 9e), respectively.

Sediment transport beyond the 25 m contour line is considered insignificant (< 5 $m^3\ m^{-1}$) in all transects when comparing with transport rates at shallower depths (Figure 9b–h). This contour is considered the maximum depth for significant sediment transport and is used as the seaward limit for sediment fluxes computation. The selection of the 25 m depth contour is also supported by seabed textural studies in this area which suggest that 20 – 26 m depth represents the base of the active profile (McCarroll et al., 2018; Valiente et al., 2019a). Moreover, this limit is also close to the average maximum depth of transport or *DoT* (c. 26 – 28 m depth) computed using tide- and wave-induced bed shear stresses during extreme conditions (Valiente et al., 2019a).

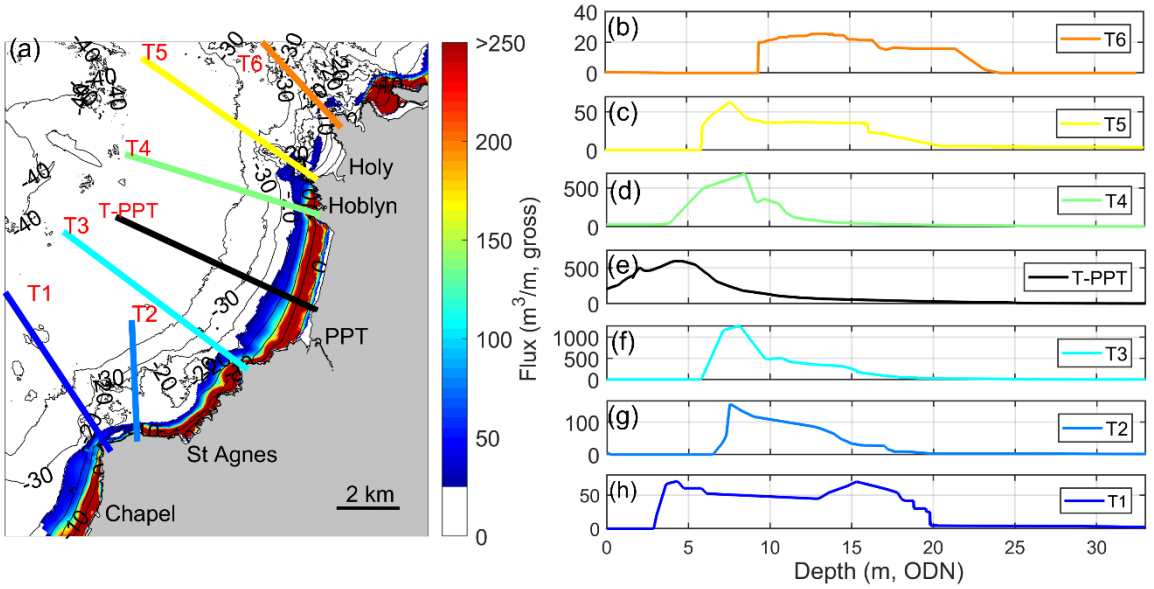

Figure 9. (a) Gross sediment transport (cumulative flux) for the simulated scenarios (total of 6 months). Gross longshore fluxes (LST_{gross}) as a function of water depth for T1 – T6 (b – d, f – h) and T-PPT (e).

4.3.2 Potential sediment transport

Time-averaged (12.5 h) sediment fluxes during moderate to high-energy wave conditions are presented spatially in Figure 10. It is evident that during storm events, major sediment fluxes occur inside the surf zone (> 8 m^3 m^{-1} s^{-1}). Sediment transport from the beach to the lower shoreface is associated with the presence of mega-rips (Figure 10a,c), generated off the southern to mid sector of all the embayments as a result of the embayment-scale (Figure 10d,e) and multi-embayment scale cellular rip cell circulation (Figure 10f). The latter occurs in Perranporth-Hoblyn's Cove system as a combined response induced by the strong offshore northward flow developed at the southern headland, high-oblique breaking and deflection of the offshore flow back toward the south at the northern headland of Hoblyn's Cove, and waves breaking beyond Ligger Point headland (northern Perranporth headland) (McCarroll et al., 2018). For moderate-high events, mega-rips induce sediment transport beyond the 15 m contour line (> 3 m^3 m^{-1} s^{-1}) and can exceed the 25 m contour line during the extreme wave events. Additionally, in the long embayments, a small rip appears at the northern headlands (Figure 10d,f); however, this rip transports much less sediment (~ 2 m^3 m^{-1} s^{-1} around 20 m depth) and is tide-dependent, disappearing with the rising tide.

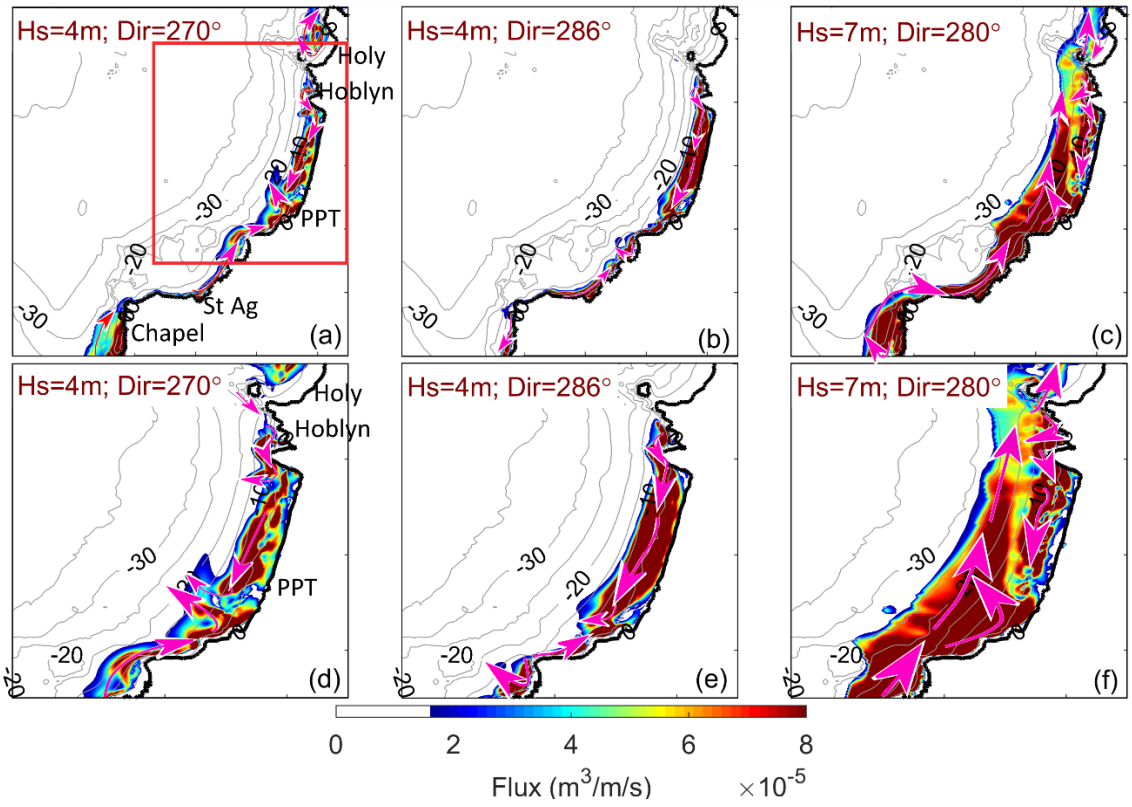

Figure 10. Sediment fluxes and transport pathways during major circulation modes (storm conditions during spring tides). Time-averaged (12.5 h) fluxes (top panels) with zoom focused on Perranporth embayment (bottom panels) under moderate-high waves from the W (a, d), WNW (b, e) and extreme waves during storm Hercules, 2013/14 winter (c, f). H_s and *Dir* presented for each scenario correspond with offshore conditions. The magenta arrows indicate qualitatively major sediment paths. For reference, embayment names abbreviations and bottom panels inset area (red box) are included in first column panels.

Headland bypass (Q_{bypass}) computed using the six transects perpendicular to the headlands (T1 – T6) and the extra transect located in the middle of Perranporth embayment (T-PPT) is presented in Figure 11. Sediment fluxes present large variability between events c. 10^2 –10^4 m^3 and always occur in the direction of the residual flow for this coast (northward), except across T4 and T-PPT. Sediment transport rates across T3 are four times larger than bypassing rates in the other headlands (Figure 11e,f). For moderate-energy and extreme conditions from the W, T3 headland bypass is $2x10^3$ m^3 (Figure 11f) and $3x10^4$ m^3 (Figure 11e), respectively, whereas transport rates are < 10^3 m^3 for moderate events coming from the WNW (weaker northward wave-induced current along the headland). In line with McCarroll et al. (2018), the largest bypassing rates at T4 are southward, and range between $-1x10^3$ and $-2x10^4$ m^3. Interestingly, despite the majority of Q_{bypass} being southward as a result of the multi-embayment cellular circulation, during the Hercules 2013/14 storm (largest simulated event; Figure 11e) the resultant net transport was $5x10^3$ m^3 northward. In this particular case, the southward transport

observed between the headland apex and 15 m depth (ODN) was compensated by the northward sediment inflow when integrated up to 25 m. It is worth noting that the specified sediment layer in the model runs provided unlimited sediment supply and uniform sediment size; therefore, the predicted rates of sediment inflows across the transects are likely to be over-estimated. Additionally, results on the bypassing rates are strongly dependent on the sediment size (D_{50} = 0.3 mm in our case) and the selected sediment transport formulation. Despite these limitations, the modelled bypassing rates suggest potentially large sediment inflows into the embayments during storm events.

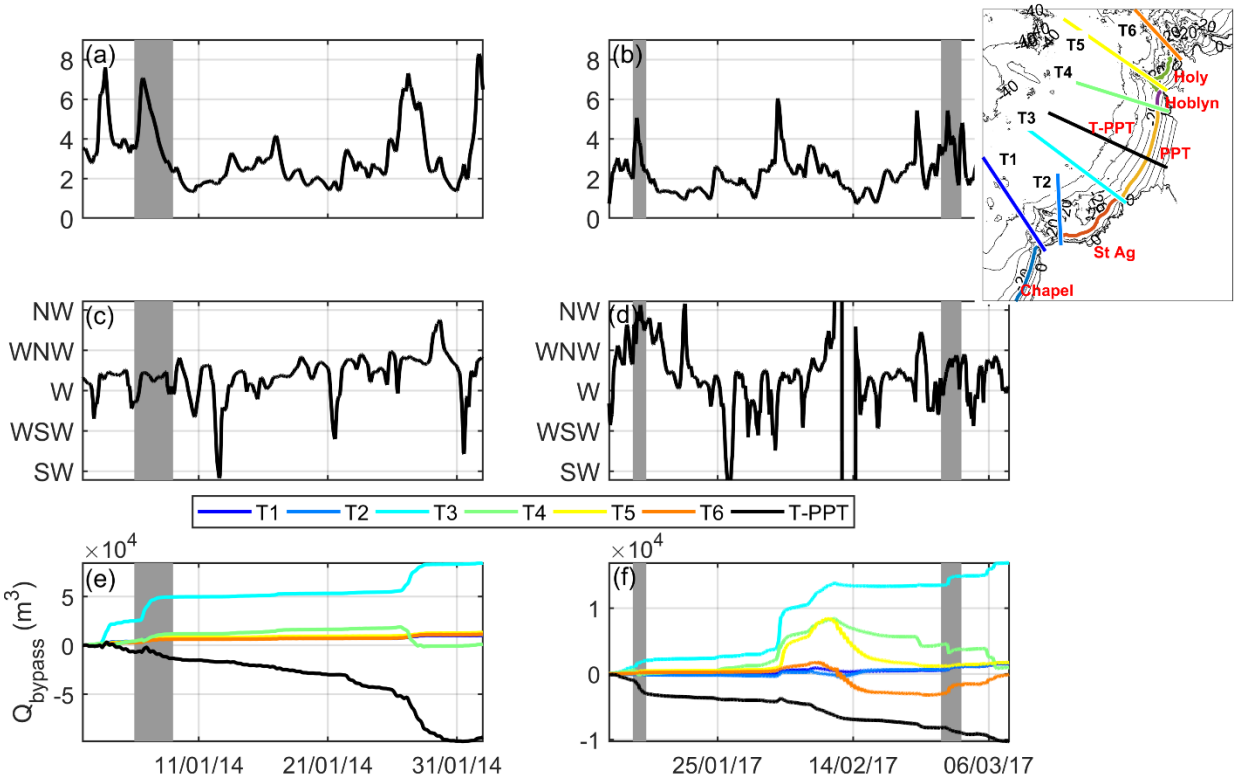

Figure 11. Sediment fluxes during major circulation modes: moderate-high waves from the W, WNW and extreme waves during storm Hercules, 2013/14 winter (bounded areas). Time series of (a, b) significant wave height (H_s); (c, d) direction (Dir); and (e, f) fluxes integrated around the headland transects (Q_{bypass}). Positive indicates northward and negative represents southward. Bounded areas represent the time period encompassing the scenarios shown in Figure 10. Inset with location of transects used for Q_{bypass} integration are presented to facilitate interpretation.

Headland (Q_{bypass}) sediment fluxes integrated over two tidal cycles (25 h) with respect to daily averages of offshore wave power (P_o) and wave angle relative to shore-normal (Θ) are shown in Figure 12. The shore-normal angles were computed using the 15 m contour line and oscillated from 320º (St. Agnes) to 280º (Perranporth-Hoblyn's Cove). Bypassing fluxes can

be considered the primary pathways for sediment exchange on the lower shoreface during conditions of maximum bed shear stress (P_o > 200 kW/m) and to a lesser extent during moderate to high-energy conditions (P_o = 75 – 125 kW/m). Their salient features are: (i) maximum longshore transport rates are c. 10^4 day^{-1} and increase with wave power; (ii) longshore transport is mostly northward, except at the two southern transects under low-to-moderate wave conditions (P_o < 70 – 80 kW/m); and (iii) wave direction relative to shore-normal seems to play a secondary role (Figure 12b), meaning that the topo-bathymetric configuration is the main control in the sediment bypassing rates. Hence, Q_{bypas} appears largely controlled by wave power (Figure 12a) and shows a strong positive correlation with Pearson correlation coefficients (r) > 0.92 in all instances. It is noted that for the particular case of T4, small variations in wave direction affect the direction of the sediment bypass (Figure 11e,f), but these appear superimposed by changes in wave power (as per McCarroll et al., 2018).

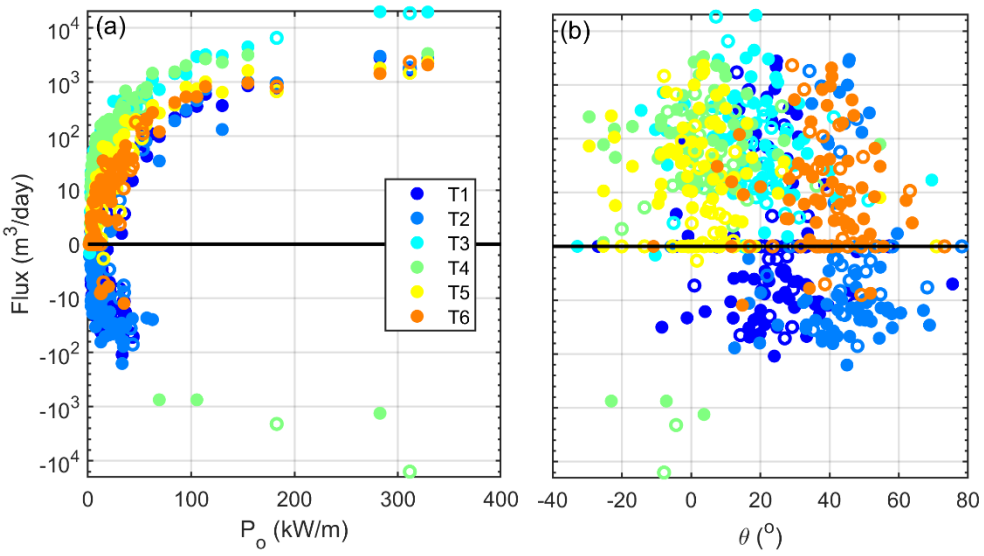

Figure 12. Daily sediment fluxes integrated over two tidal cycles (25 h) versus daily averages of offshore wave power (*Po*) and wave angle relative to shore-normal (*Θ*). Sediment fluxes are integrated over the selected transects (refer to Figure 1 for location) with positive values corresponding to northward fluxes and negative to southward. Empty circles represent sea states during neap tides whereas filled markers depict spring tides. *Θ* counter-clockwise from shore-normal are positive.

5 Discussion

5.1 Sediment transport mechanisms

A conceptual model of headland bypassing and major sediment transport pathways for increasing wave forcing conditions (H_s = 0 – 2 m, 2 – 5 m, > 5 m) along an idealised embayed

coastline based on the study area in SW England with two types of embayment lengths is shown in Figure 13. Major mechanisms for redistributing material to and along the lower shoreface for embayed coastlines are the longshore flow around headlands (northward for SW England), the presence of mega-rips, and the embayment-scale circulation (clockwise for SW England). Both embayment-scale circulation and headland bypass are a function of wave obliquity, embayment length and headland configuration (Martens et al., 1999; Short and Masselink, 1999).

The residual tidal flow, northward for the particular case of the N coast of SW England (Valiente et al., 2019a; King et al., 2019), is enhanced by a strong (~1 m s^{-1}) wave-induced current near the headland produced by oblique wave breaking during moderate (Figure 13b-i) to high energy conditions (Figure 13c-i). This alongshore flow is diverted offshore as a strong mega-rip (c. 0.7 m s^{-1} at 20 m depth ODN) at the down-wave headlands which may constitute a pathway for sediment ejection beyond the offshore morphological embayment limit in the southern sectors. In line with Castelle and Coco (2013), this mechanism is more evident at longer beaches (e.g., Perranporth and Chapel Porth) in which a longshore current meandering over the bar and rips has enough room to develop, deflecting further offshore the alongshore flow diverting as a mega-rip. This mechanism for flushing material through the headland rips has been observed in other swell-dominated headland-bound beaches (Gallop et al., 2011; Loureiro et al, 2012; McCarroll et al., 2014), revealing that a significant amount of sediment can be ejected outside the surf zone during extreme events.

Modelled headland bypass (Figure 13b,c-ii) was mostly northward. In line with George et al. (2019), this headland bypass is almost absent at the sharp headlands that act as a quasi-impermeable barrier to littoral drift. Conversely, in headlands with a wide apex and an up-face – side of the headland from which the wave-induced flow would travel – almost parallel to the direction of the wave approach (e.g., Cligga Head) important northward headland bypass (10^3 – 10^4 m^3 day^{-1}) during moderate to large waves occurs, and this is similar to other high-energy embayed coastlines (Vieira da Silva et al., 2018). This headland bypass is still present during low-energy wave conditions but is more subdued (<< 10^2 m^3 day^{-1}). Over the long term, this mechanism will cause slow accretion in embayments with a downdrift sharp headland, and slow erosion in embayments with a downdrift wide headland. For the particular case of Ligger Point (Perranporth northern headland), when multi-embayment circulation develops (Figure 13b,c-iv) during extreme wave conditions (McCarroll et al., 2018), southward headland bypass from Hoblyn's Cove to Perranporth occurs.

Clockwise embayment-scale circulation (Figure 13b-iii) is predicted to occur over moderate-high swell periods. This circulation mode induces a slow intra-embayment sediment transport from the up-wave to the down-wave part of all the embayments (cf. Castelle and Coco, 2012). This circulation mode arises from the interaction between the wave-driven current and tidal residual flow, and the geometry and orientation of the bounding headlands. For the particular case of the SW, the northward alongshore current (beyond -10 m ODN) is deflected onshore at the north and is aided by an onshore flow generated by high-oblique breaking waves along the north headland. The combination of both mechanisms forces an intra-embayment sediment redistribution along the lower shoreface towards the south of c. 10^2 – 10^3 m^3 day^{-1}, contributing to sediment gains over mild winter periods. As a result of this circulation, bypassing at the short headlands (Figure 13b-iii) occurs, although is much weaker than the bypassing rates during extreme events and is also partially conditioned by the obliquity of the waves.

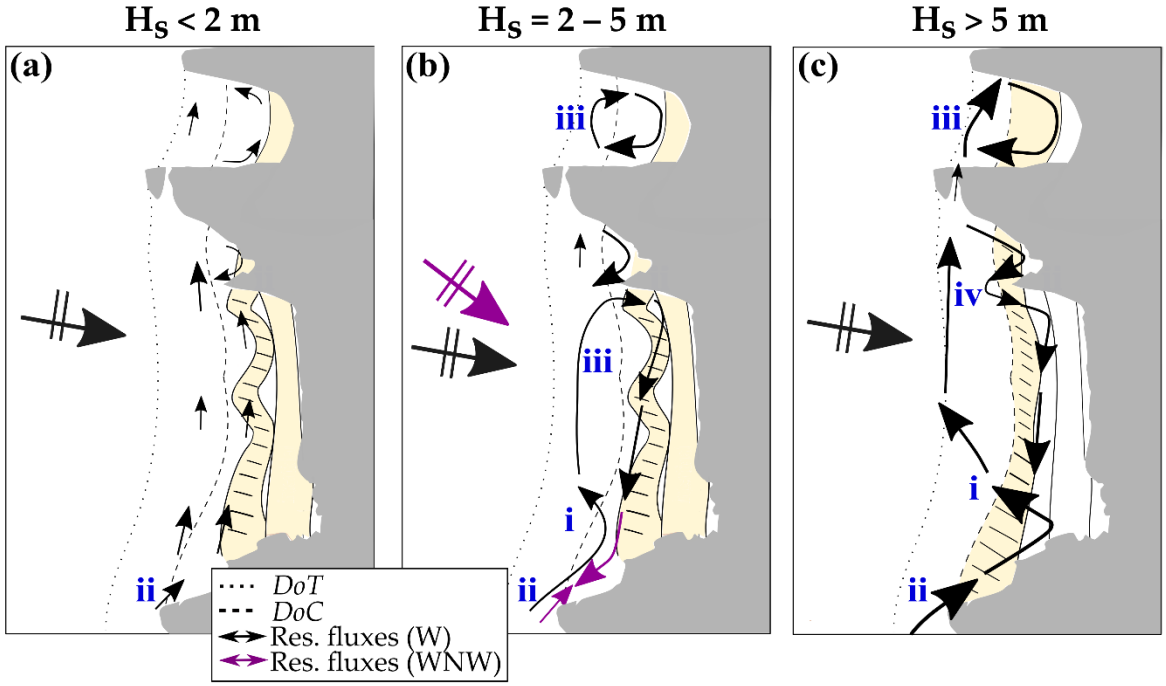

Figure 13. Conceptual diagram of major alongshore sediment fluxes pathways for a period of (a) mild waves, (b) moderate-high waves and (c) higher than average wave. Arrows (size increases with increasing magnitude) indicate predicted residual fluxes based on model output. Accretion due to cross-shore fluxes from Valiente et al. (2019b) is shown in beige. Idealised limits of the active shoreface Depth of Transport (*DoT*) and Depth of Closure (*DoC*) following Valiente et al. (2019a) are presented as dot and dashed lines, respectively.

5.2 Prediction of bypassing rates and sediment budgets

This research has shown that substantial sediment transport along the lower shoreface related to headland bypassing mechanisms may occur under the assumption of unlimited sediment supply at the N coast of SW England. Furthermore, the modelled sediment bypass fluxes were found to be positively correlated ($r > 0.92$) with offshore wave power (P_o), allowing for a simple parameterisation of the headland bypassing rates. The approach followed here to obtain a daily bypass rate parameterisation (Q_{bypass}, in m^3 day^{-1}) is simply based on curve fitting using a second order linear model polynomial of the form:

$$Q_{bypass} = aP_o^2 + bP_o + c \quad (1)$$

where P_o is the daily averaged offshore wave power estimated using Herbich (2000), and *a*, *b* and *c* (Table 3) are the best fitting parameters based on the correlation between model output sediment fluxes and wave power forcing conditions at the offshore boundary of the domain (location A, refer to Figure 1a). Using Ligger Point as case study, McCarroll et al. (2018) also provided a Q_{bypass} parameter. This parameter accounted for the tidal residual current while allowing for resolution of changes in wave energy and direction, whereas our approach only relies on total wave energy while addressing the bypass reversal during large energy waves (T4, a = -0.2; Table 3). McCarroll et al. (2018) demonstrates that the contribution of the tide can be considered secondary (only noticeable for values of bypassing < 100 m^3 day^{-1} during spring tides) and corresponds to < 5% of the total bypass. These authors simulate synoptic scenarios and use a single headland of the North coast of Cornwall (equivalent to T4 in this study), whereas our study focuses in the simulation of hindcasted conditions in six headlands. McCarroll et al. (2018) predicted maximum bypassing rates around one specific headland of c. 10^4 m^3 day^{-1} southward, which is comparable to the results of our parameterisation based on curve fitting.

Table 3. Best fitting parameters for Eq. 1 based on correlation between modelled sediment fluxes and offshore wave forcing conditions.

Transect	*a*	*b*	*c*
T1 – St. Agnes Head	0.0171	1.85	-40.12
T2 – St. Agnes Head	0.01255	2.54	-26.14
T3 – Cligga Head	0.1883	2.99	-31
T4 – Ligger Point	-0.2009	31.72	-317
T5 – Penhale Point	0.0009	6.06	-62
T6 – Kelsey Head	0.0125	2.54	-26.14

Following the proposed parameterisation (Eq. 1), a hindcast of the sediment inflows and outflows for the different embayments of study at multi-annual timescales is conducted. In all transects, headland bypass is northward (except for T4) and becomes significant ($10^3 – 10^5$ m^3) over winter periods, with maximum predicted values during high energy summer conditions of 10^3 m^3. Examining T4 individually, we found that the cumulative Q_{bypass} is northward, but conversely to the other headlands, the 2013/14 winter storms and to a lesser extent winters 2015/16 and 2017/18 induced a net southward bypass as a result of the multi-embayment circulation. This is consistent with McCarroll et al. (2018), who predicted bypass rates for a transect similar to T4, showing similar reversals in flux direction at higher wave-energy levels, with net near-zero long-term flux (with wide uncertainty bounds), including gradual northward flux in summer, and brief periods of rapid southward transport in winter.

The introduction of the Q_{bypass} parameter allows quantifying sediment bypass over long timescales (multi-annual) and can provide of a quick and rough estimate of sediment budgets. Following the proposed parameterisation (Eq. 1), a prediction of the sediment inflows and outflows for the different embayments of study at multi-annual timescales is conducted. For a given coastal cell, the sediment budget (dQ_{net}) is expressed by the balance of volumes between sediment supply (ΣQ_{source}) and sediment losses (ΣQ_{sink}) in the compartment (Rosati, 2005; Aagaard, 2011). Hence, Q_{bypass} of a particular headland provides sediment losses (gains) to the updrift (downdrift) bay. For the studied stretch of coast, assuming that ΣQ_{source} through the southern updrift boundary is equal to zero (virtual zero), and knowing the sediment sources ($Q_{bypass,up} = \Sigma Q_{source}$) and gains ($Q_{bypass,down} = \Sigma Q_{sink}$) of each study bay, we are able to infer the sediment budget over a particular timescale (dQ_{net}/dt).

Figure 14 shows the predicted total sediment budgets and net headland bypassing (Q_{bypass}) over an 8-year period (2011 – 2018). For two (Perranporth and Holywell) of the five embayments, sediment gains are larger than sediment losses ($\Sigma Q_{source} > \Sigma Q_{sink}$) over multi-annual scales. For the studied 2011 – 2018 epoch, the Perranporth embayment sediment budget ($Q_{bypass,up}$ and $Q_{bypass,down}$ are c. 1.2×10^6 m^3 and 1.3×10^5 m^3, respectively) is one order of magnitude larger than for Holywell (Figure 14a). Additionally, major circulation paths during large events suggest that the northern headland (Ligger Point) acts as a secondary headland, converting Hoblyn's Cove into an extension of Perranporth beach, and Penhale Point into Perranporth-Hoblyn's Cove major headland. Because northward bypass fluxes at Penhale Point

(Figure 14a) are one order of magnitude (c. $2.4x10^5$ m^3) smaller than those predicted for Cligga Head (southern updrift headland), it is suggested that Perranporth-Hoblyn's cove multi-embayment system is in permanent accretion (> $1x10^6$ m^3 over 8 years) if an unlimited sediment supply from the updrift coastal section existed, which is unlikely to be the case. For this same epoch (2011 – 2018), Valiente et al. (2019b) observational study suggested that Perranporth beach accreted > 650,000 m^3 when accounting for changes up to 30-m depth. A comparison against these observations suggest that although Perranporth-Hoblyn's cove may act as a sink for a major coastal cell (Figure 14b) over the long term, the predicted total sediment budget based on bypassing rates presented here certainly represents a very upper bound. Thus, the sediment budgets estimate is a useful tool for finding hotspots that are more vulnerable to experience lack of sediment supply in the long term, but currently has limited predictive capacity. This sediment budget hindcast assumes unlimited sediment supply updrift; therefore, results of bypass should be interpreted with caution as the cumulative magnitude presented here is not sustainable for a sediment-starved region.

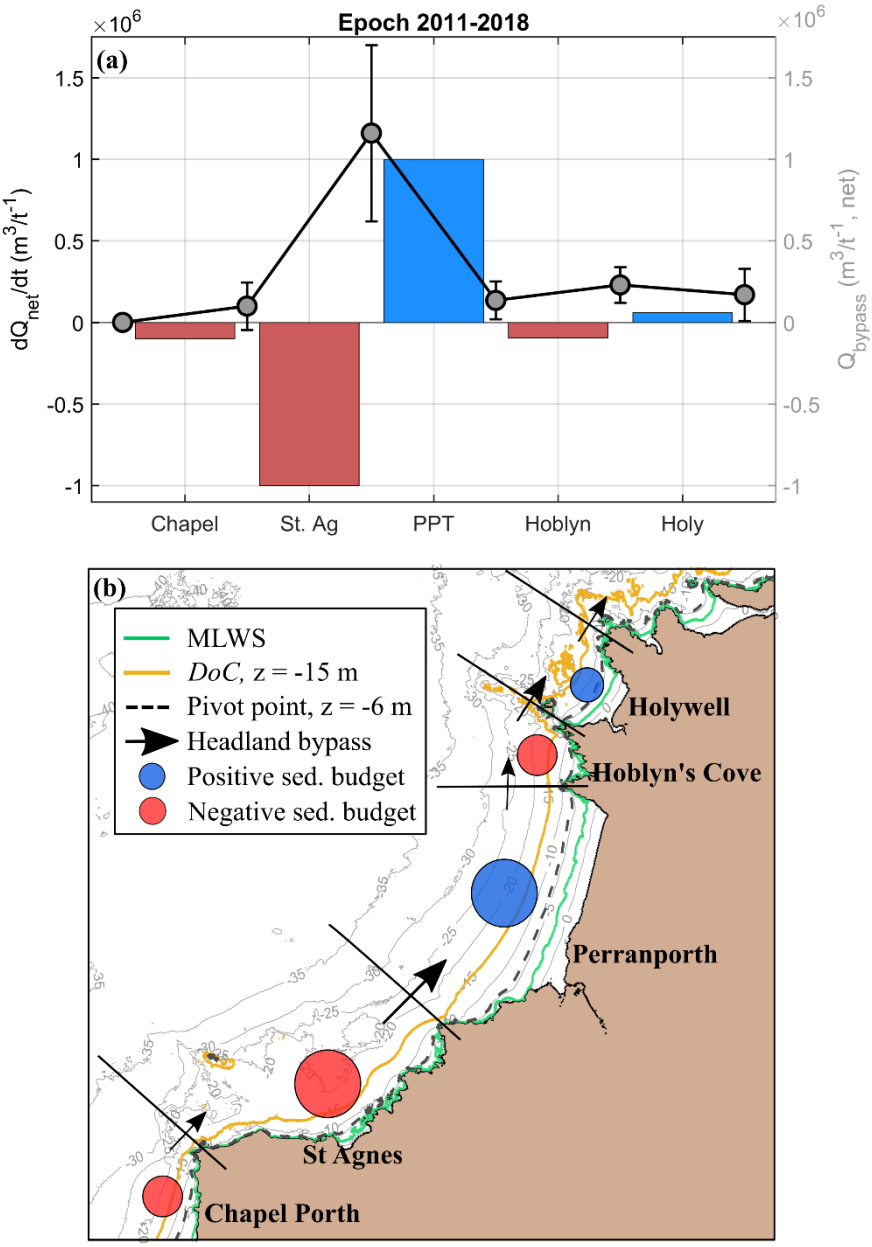

Figure 14. (a) Predicted total sediment budgets (dQ_{net}/dt) and net headland bypassing (Q_{bypass}) and associated uncertainty bounds (95% confidence based on the statistical model). (b) Planform sediment budget model for Chapel Porth, St. Agnes, Perranporth, Hoblyn's Cove and Holywell over 2011 – 2018. Arrows indicate qualitatively net headland bypassing paths. Arrows and circles size represents magnitude.

Recent modelling studies provided sediment transport prediction around artificial coastal structures (Ab Razak et al., 2013), and natural (Vieira da Silva et al., 2016, 2018; McCarroll et al., 2018, 2019) and idealised (George et al., 2019) headlands. These works computed and parameterised (e.g., McCarroll et al., 2018; George et al., 2019) bypassing rates around different headlands accounting for certain embayment circulation control. Our study provides similar results in terms of bypassing rates during energetic periods (order of 10^3 – 10^4 m^3 y^{-1});

however, we also show possible bypassing rates of 10^5 m^3 y^{-1} during exceptionally energetic years (e.g., winter 2013/2014; Masselink et al., 2016a,b), and add a more robust understanding of the embayment- and multi-embayment-scale sediment dynamics and complex circulation for long embayments.

It is suggested that beaches on this coastline form part of an extended coastal cell, with individual embayments linked via sediment transport around headlands. This type of coastline was previously thought to be only dominated by cross-shore fluxes (Scott et al., 2016; Masselink et al., 2016b; Burvingt et al., 2017) as the embayments were studied partially and disagreements between the different sectors of the subtidal systems were never observed up to the study of Valiente et al. (2019b). The present work predicts that longshore sediment transport rates can potentially be of the same order of magnitude (maximum bypassing rates 10^5 m^3 y^{-1}) than the observed maximum cross-shore fluxes (Valiente et al., 2019b). Additionally, despite Valiente et al. (2019b) demonstrating that upper shoreface sediment fluctuations are uncorrelated to lower shoreface response at short-mid temporal scale, the magnitude of the longshore fluxes presented here will certainly condition the upper shoreface (beach) response at longer timescales (> 10 years). Consequently, lower shoreface alongshore fluctuations in the rate of transport seem a critical mechanism which should be considered when studying long-term beach evolution, specifically along high energy and sediment starved coastlines.

6 Conclusions

This study presents a numerical modelling investigation of the processes redistributing material along the lower shoreface of a complex high-energy embayed coastline. Numerical simulations of wave- and tide-induced currents were used to model the main sediment transport pathways and potential sediment fluxes due to headland bypassing at event to multi-annual timescales. This study provides an order of magnitude analysis of sediment bypassing rates both around headlands and intra-embayment using hindcasted forcing conditions, where:

- Primary sediment transport mechanisms in the lower shoreface of headland-bound beaches are longshore residual flow (induced by waves and tide) to mega-rip, headland bypass and headland rip cell circulation, with the latter a function of embayment length, headland configuration and wave obliquity.
- Periods with moderate-high swell (H_s ~ 4 m) are associated with accretionary phases and net sediment gains. The main sediment paths during these periods arises from the clockwise intra-embayment circulation where predicted currents induce

redistribution in the long embayments (> 10^3 m^3 day^{-1}) towards the south contributing to sediment gains. The intra-embayment sediment redistribution is combined with significant bypassing rates around the shallower and wider headlands (10^2 – 10^3 m^3 day^{-1}).

- Both multi-embayment circulation and large sediment fluxes beyond the bounding headlands (> 10^4 m^3 day^{-1}) dominate during extreme events (Hs ~ 7 m). This circulation mode can encompass several systems when bounded by relatively-shallow headlands, and is associated with significant movement of sediment offshore. Furthermore, the large sediment fluxes are likely to be linked to the longshore flow to mega-rip formation (0.7 m s^{-1} at > 20 m depth) occurring in the southern sector (down-wave) of the long embayments.

A second order polynomial of the relationship between offshore wave-conditions and modelled sediment bypass is presented for the SW of England, allowing site-specific estimation of the magnitude of sediment fluxes on the lower shoreface over multi-annual timescales. Hindcast of sediment transport rates in this coastal section suggests that major sediment fluxes are episodic and occur up to the 25 m contour line, mainly during high-energy events. Additionally, this seaward depth for significant sediment transport matches seabed textural changes in the main embayments. During extreme events, bypass around the headlands can reach 10^4 m^3 day^{-1}, whereas for moderate wave conditions, headland bypassing is at least one order of magnitude smaller (10^2 – 10^3 m^3 day^{-1}). Finally, positive net sediment rates over 2011 – 2018 suggested that Perranporth-Hoblyn's Cove system could potentially act as a sink for the N coast of SW England.

Our study highlights the importance of sediment transport estimates along the lower shoreface, which remains a poorly understood area of the coastal system. Additionally, the predicted sediment fluxes in the sub-tidal sector provide new insights into a coastline previously thought to be dominated by cross-shore sediment fluxes. Yearly bypassing rates around the headlands are hindcasted ranging between 10^3 and 10^5 m^3 y^{-1}. Despite the fact that these fluxes represent an upper bound estimate due to the numerous assumptions in the model design, the magnitude of the predicted bypass will inevitably affect evolution of rocky coastlines over longer temporal scales (> 10 years). This work demonstrates that headland

bypassing is more widespread than commonly assumed, leading to a shift in understanding of sediment budgets along exposed and macrotidal headland-bound beaches.

Acknowledgments

This work was supported by UK Natural Environment Research Council grant (NE/M004996/1; BLUE-coast project), and by EPSRC through an Overseas Travel Grant awarded to GM (Coastal modelling of extreme storms and sea-level rise; EP/T004304/1). Thank you to all those who assisted with the ADCP deployment, in particular Peter Ganderton and Aaron Barrett. Wave and bathymetric data were provided by the Plymouth Coastal Observatory (PCO) and United Kingdom Hydrographic Office (UKHO), respectively. Special thanks to Andy Saulter for providing Met Office Wave Watch III data.

References

Aagaard, T. (2011). Sediment transfer from beach to shoreface: The sediment budget of an accreting beach on the Danish North Sea Coast. *Geomorphology*, 135(1–2), 143–157. https://doi.org/10.1016/j.geomorph.2011.08.012

Ab Razak, M. S., Dastgheib, A., Roelvink, D. (2013). Sand bypassing and shoreline evolution near coastal structure, comparing analytical solution and XBeach numerical modelling. *Journal of Coastal Research*, 65(2), 2083–2088.

Bakhtyar, R., Dastgheib, A., Roelvink, D., Barry, D. A. (2016). Impacts of wave and tidal forcing on 3D nearshore processes on natural beaches. Part I: Flow and turbulence fields. *Ocean Systems Engineering*, 6(1), 23–60.

Booij, N., Ris, R. C., Holthuijsen, L. H. (1999). A third-generation wave model for coastal regions 1. Model description and validation. *Journal of Geophysical Research*, 104 (C4), 7649–7666.

Bricheno, L. M., Wolf, J., Aldridge, J. (2015). Distribution of natural disturbance due to wave and tidal bed currents around the UK. *Continental Shelf Research*, 109, 67–77. https://doi.org/10.1016/j.csr.2015.09.013

Brown, J. M., Phelps, J. J. C., Barkwith, A., Hurst, M. D., Ellis, M. A., Plater, A. J. (2016). The effectiveness of beach mega-nourishment, assessed over three management epochs. *Journal of Environmental Management*, 184 (2), 400–408.

Bruciaferri, D., Shapiro, G., Stanichny, S., Zatsepin, A., Ezer, T., Wobus, F., Francis, X., Hilton, D., 2020. The development of a 3D computational mesh to improve the representation of dynamic processes: the Black Sea test case. Ocean Model 146, 101534. https://doi.org/10.1016/j.ocemod.2019.101534.

Burvingt, O., Masselink, G., Russell, P., Scott, T. (2017). Classification of beach response to extreme storms. *Geomorphology*, *295*, 722–737. https://doi.org/10.1016/j.geomorph.2017.07.022

Castelle, B., Coco, G. (2012). The morphodynamics of rip channels on embayed beaches. *Continental Shelf Research*, *43*, 10–23. https://doi.org/10.1016/j.csr.2012.04.010

Castelle, B., Coco, G. (2013). Surf zone flushing on embayed beaches. *Geophysical Research Letters*, 40(10), 2206–2210. https://doi.org/10.1002/grl.50485

Castelle, B., T. Scott, R. W. Brander, R. J. McCarroll (2016). Rip-current types, circulation and hazard. *Earth Science Reviews*, 163, 1–21. doi: 10.1016/j.earscirev.2016.09.008.

Deltares (2014). Delft3D-FLOW User Manual Hydro-Morphodynamics., pp. 710.

Duarte, J., Taborda, R., Ribeiro, M., Cascalho, J., Silva, A., and Bosnic, I. (2014). Evidences of sediment bypassing at Nazare headland revealed by a large scale sand tracer experiment, *Jornadas de Engenharia Hidrografica*, Lisboa 24-26 de junho 2014, pp 289:292

Elias, E.P.L. (2018). Bench-mark morphodynamic model Ameland Inlet - Kustgenese 2.0 (ZG-C2), Deltares, Project 1220339-008, Reference 1220339-008-ZKS-0001, 70 pp.

Gallop, S. L., Bryan, K. R., Coco, G., Stephens, S. A. (2011). Storm-driven changes in rip channel patterns on an embayed beach. *Geomorphology,* 127, 179-188.

George, D. A., Largier, J. L., Storlazzi, C. D., Robart, M. J., and Gaylord, B. (2018). Currents, waves and sediment transport around the headland of Pt. Dume, California. *Continental Shelf Research*, *171*, 63–76. https://doi.org/10.1016/j.csr.2018.10.011

George, D.A., Largier, J.L., Pasternack, G. B., Barnard, P. L., Storlazzi, C.D., Erikson, L. H. (2019). Modeling Sediment Bypassing around Idealized Rocky Headlands. *Journal of Marine Science and Engineering*, 7, 40. doi:10.3390/jmse7020040

Giardino, A., Briere, C. D. E., Van der Werf, J. J. (2011). Morphological Modelling of Bar Dynamics with Delft3d. The Quest for Optimal Parameter Settings, Tech. Rep. 1202345–000, Deltares.

Goodwin, I. D., Freeman, R., Blackmore, K. (2013). An insight into headland sand bypassing and wave climate variability from shoreface bathymetric change at Byron Bay, New South Wales, Australia. *Marine Geology*, *341*, 29–45. https://doi.org/10.1016/j.margeo.2013.05.005

Goring, D. G., Nikora, V. I. (2002). Despiking Acoustic Doppler Velocimeter Data. *Journal of Hydraulic Engineering*, *128*(1), 117–126. https://doi.org/10.1061/(asce)0733-9429(2002)128:1(117)

Grunnet, N. M., Walstra, D. J. R., Ruessink, B. G. (2004). Process-based modelling of a shoreface nourishment. *Coastal Engineering*, *51*(7), 581–607. https://doi.org/10.1016/j.coastaleng.2004.07.016

Hansen, J. E., Elias, E., List, J. H., Erikson, L. H., Barnard, P. L. (2013). Tidally influenced alongshore circulation at an inlet-adjacent shoreline. *Continental Shelf Research*, 56, 26–38. https://doi.org/10.1016/j.csr.2013

Herbich, J. B. (2000). *Handbook of Coastal Engineering.* McGraw-Hill Professional, New York City, USA.

Holt, J. T., James, I. D., Jones, E. J. (2001). An s coordinate density evolving model of the northwest European continental shelf: 2. Seasonal currents and tides. *Journal of Geophysical Research*, 106(C7), 14,035–14,053. https://doi.org/10.1029/2000JC000303

Hopkins, J., Elgar, S., Raubenheimer, B. (2015). Observations and model simulations of wave-current interaction on the inner shelf. *Journal of Geophysical Research: Oceans*, 121, 198–208. https://doi.org/10.1002/2015JC010788

Huisman, B.J.A., Ruessink, B.G., de Schipper, M.A., Luijendijk, A.P., Strive, M.J.F., 2019. Modelling of bed sediment composition changes at the lower shoreface of the Sand Motor. Coastal Engineering 132, 33–49.

Hsu, Y. L., Dykes, J. D., Allard, R. A., Kaihatu, J. M. (2006). Evaluation of Delft3D Performance in Nearshore Flows, NRL memorandum report, NRL/MR/7320-06-8984, 24 pp.

Kara, A. B., Rochford, P. A., Hurlburt, H. E. (2000). An optimal definition for the ocean mixed layer depth, *Journal of Geophysical Research: Oceans*, 105(C7). https://doi.org/10.1029/2000JC900072 King, E., Conley, D., Masselink, G., Leonardi, N., McCarroll, R. J., Scott, T. (2019). The Impact of Waves and Tides on Residual Sand Transport on a Sediment-poor, Energetic and Macrotidal Continental Shelf. *Journal Geophysical Research Ocean*, 124, 4974–5002. https://doi.org/10.1029/2018JC014861

King, E., Conley, D., Masselink, G., Leonardi, N., McCarroll, R.J., Scott, T., 2019. The Impact of Waves and Tides on Residual Sand Transport on a Sediment-poor, Energetic and Macrotidal Continental Shelf. Journal Geophysical Research Ocean 124, 4974–5002. https://doi.org/10.1029/2018JC014861.

Komar, P. D. (1998). Beach processes and sedimentation. Prentice-Hall, Inc., Simon and Schuster, Upper Saddle River, NJ, pp. 66–72.

Komen, G. J., Hasselmann, S., Hasselmann, K. (1984). On the existence of a fully developed wind-sea spectrum. *Journal of* Physical *Oceanography*, 14, 1271–1285.

Loureiro, C., Ferreira, Ó., Cooper, J. A. G. (2012a). Extreme erosion on high-energy embayed beaches: Influence of megarips and storm grouping. *Geomorphology*, *139–140*, 155–171. https://doi.org/10.1016/j.geomorph.2011.10.013

Luijendijk, A. P., Ranasinghe, R., de Schipper, M. A., Huisman, B. A., Swinkels, C. M., Walstra, D. J. R., Stive, M. J. F. (2017). The initial morphological response of the Sand Engine: A process-based modelling study. *Coastal Engineering*, *119*, 1–14. https://doi.org/10.1016/j.coastaleng.2016.09.005

Lyddon, C., Brown, J. M., Leonardi, N., Plater, A. J. (2018). Flood hazard assessment for a hyper-tidal estuary as a function of tide-surgemorphology interaction. *Estuaries and Coasts*, 41(6), 1565–1586. https://doi.org/10.1007/s12237-018-0384-9

Madec, G. and the NEMO System Team, 2016. "NEMO ocean engine", Scientific Notes of Climate Modelling Center (27) – ISSN 1288-1619, Institut Pierre-Simon Laplace (IPSL), France. doi=10.5281/zenodo.1464816

Martens, D., Williams, T., Cowell, P. (1999). Mega-rip dimensional analysis on the Sydney coast Australia, and implications for beach-state recognition and prediction. *Journal of Coastal Research,* 17, 34–42.

Masselink, G., Austin, M., Scott, T., Poate, T., Russell, P. (2014). Role of wave forcing, storms and NAO in outer bar dynamics on a high-energy, macro-tidal beach. *Geomorphology*, *226*, 76–93. https://doi.org/10.1016/j.geomorph.2014.07.025

Masselink, G., Castelle, B., Scott, T., Dodet, G., Suanez, S., Jackson, D., Floc, F. (2016a). Extreme wave activity during 2013/2014 winter and morphological impacts along the Atlantic coast of Europe. *Geophysical Research Letters*, 2135–2143.

Masselink, G., Scott, T., Poate, T., Russell, P., Davidson, M., Conley, D. (2016b). The extreme 2013/14 winter-storms: Hydrodynamic forcing and coastal response along the southwest coast of England. *Earth Surface Processes and Landforms*, 41(3), 378–391. https://doi.org/10.1002/esp.3836

McCarroll, R.J., Brander, R.W., Turner, I.L., Power, H.E., Mortlock, T.R. (2014). Lagrangian observations of circulation on an embayed beach with headland rip currents. *Marine Geology*, 355, 173–188.

McCarroll, R. J., Brander, R. W., Turner, I. L., Leeuwen, B. Van. (2016). Shoreface storm morphodynamics and mega-rip evolution at an embayed beach: Bondi Beach, NSW, Australia. *Continental Shelf Research*, *116*, 74–88. https://doi.org/10.1016/j.csr.2016.01.013

McCarroll, R., Masselink, G., Valiente, N., Scott, T., King, E., Conley, D. (2018). Wave and Tidal Controls on Embayment Circulation and Headland Bypassing for an Exposed, Macrotidal Site. *Journal of Marine Science and Engineering*, *6*(3), 94. https://doi.org/10.3390/jmse6030094

McCarroll, R., Masselink, G., Wiggins, M., Scott, T., Billson, O., Conley, D., Valiente, N. (2019). High-efficiency gravel longshore sediment transport and headland bypassing over an extreme wave event. *Earth Surface Processes and Landforms*, 44(13). https://doi.org/10.1002/esp.4692

Mogensen, K.S., Balmaseda, M.A., Weaver, A., Martin, M., Vidard, A., 2012. NEMOVAR: A variational data assimilationsystem for the NEMO ocean model. In: ECMWF Newsletter, No.120. ECMWF, Reading, United Kingdom, pp. 17–21. http://www.ecmwf.int/sites/default/files/elibrary/2009/14605-newsletter-no120-summer-2009.pdf.

Niedonora, A.W., Swift, D.J.P., 1981. Maintenance of the shoreface by wave orbital currents and mean flow: observations from the Long Island Coast. Geophysical Research Letters 8 (4), 337–340.

O'Dea, E., Arnold, A K., Edwards, K P, Furner, R, Hyder, P, Martin, M J, Siddorn, J R, Storkey, D, While, J, Holt, J T, Liu, H. (2012) An operational ocean forecast system incorporating NEMO and SST data assimilation for the tidally driven European North-West shelf. *Journal of Operational Oceanography*, 5:1, 3-17, DOI: 10.1080/1755876X.2012.11020128

O'Dea, E., Furner, R., Wakelin, S., Siddorn, J., While, J., Sykes, P., King, R., Holt, J., Hewitt, H. (2017). The CO5 configuration of the 7 km Atlantic Margin Model: large-scale biases and sensitivity to forcing, physics options and vertical resolution. *Geosci. Model Dev*., 10, 2947–2969, https://doi.org/10.5194/gmd-10-2947-2017, 2017.

Plant, N. G., Holland, K. T, Puleo, J. A. (2002). Analysis of the scale errors in nearshore bathymetric data. *Marine Geology*, 191(1–2), 71–86. DOI: 10.1016/S0025-3227(02)00497-8

Prodger, S., Russell, P., Davidson, M. (2017). Grain-size distributions on high energy sandy beaches and their relation to wave dissipation. *Sedimentology*, 1289–1302. https://doi.org/10.1111/sed.12353

Qinghua Ye, Morelissen, R., De Goede, E., Van Ormondt, M., Van Kester, J. (2011). A New Technique for Nested Boundary. *Proceedings of the Sixth International Conference on Asian and Pacific Coasts*. https://doi.org/10.1142/9789814366489

Ridderinkhof, W., Swart, H. E., Vegt, M., Hoekstra, P. (2016). Modeling the growth and migration of sandy shoals on ebb-tidal deltas. *Journal of Geophysical Research: Earth Surface*, 121, 1351–1372. https://doi.org/10.1002/2016JF003823

Roelvink, J.A. and Van Banning, G. K. F. M. (1994). Design and Development of DELFT3D and Application to Coastal Morphodynamics. In: Verwey, A., Minns, A.W., Babovic, V. and Maksimovic, C., Eds., Hydroinformatics, Balkema, Rotterdam, 451-456.

Rosati, J. D. (2006). Concepts in Sediment Budgets. *Journal of Coastal Research*, *212*(1966), 307–322. https://doi.org/10.2112/02-475a.1

Scott, T., Masselink, G., O'Hare, T., Saulter, A., Poate, T., Russell, P., Davidson, M., Conley, D. (2016). The extreme 2013/2014 winter storms: Beach recovery along the southwest coast of England. *Marine Geology*, *382*, 224–241. https://doi.org/10.1016/j.margeo.2016.10.011

Sharples, J., Holt, J., Dye, S. R. (2013). Impacts of climate change on shelf sea stratification. *MCCIP Science Review*, 67–70. doi:10.14465/2013.arc08.067-070

Short, A.D., 1985. Rip-current type, spacing and persistence, Narrabeen Beach, Australia.Marine Geology 65 (1–2), 47–71.

Short, A. D. (2010). Role of geological inheritance in Australian beach morphodynamics. *Coastal Engineering*, *57*(2), 92–97. https://doi.org/10.1016/j.coastaleng.2009.09.005

Short, A. D., Masselink, G. (1999). Embayed and structurally controlled beaches. In A. D. (Ed. A. Short (Ed.), *Handbook of Beach and Shoreface Morphodynamics* (pp. 230–249). Chichester: John Wiley and Sons.

Sibson, R. (1981). "A Brief Description of Natural Neighbor Interpolation," chapter 2. In Interpolating Multivariate Data. New York: John Wiley and Sons, 21–36.

Thom, B. G., Eliot, I., Eliot, M., Harvey, N., Rissik, D., Sharples, C., Short, A. D., Woodroffe, C. D. (2018). National sediment compartment framework for Australian coastal management, *Ocean and Coastal Management*, 154 103-120.

Tonani, M., Blockley, E., Renshaw, R., Wakelin, S., Mahdon, R., O'Dea, E., Tinker, J. (2019). North-West Shelf CMEMS reanalysis - quality information document. Tech. rep., p. 4.2, https://resources.marine.copernicus.eu/documents/QUID/CMEMS-NWS-QUID-004-009.pdf

Valiente, N. G., Masselink, G., Scott, T., Conley, D., McCarroll, R. J. (2019a). Role of waves and tides on depth of closure and potential for headland bypassing. *Marine Geology*, *407*, 60–75. https://doi.org/10.1016/j.margeo.2018.10.009

Valiente, N.G., Masselink, G., Scott, T., McCarroll, J., Wiggins, M. (2019b). Multi-annual embayment sediment dynamics involving headland bypassing and sediment exchange across the depth of closure, *Geomorphology*, 343, 48–64. https://doi.org/10.1016/j.geomorph.2019.06.020.

van Rijn, L. C., Walstra, D. J. R., van Ormondt, M. (2004). Description of TRANSPOR2004 and implementation in Delft3D-ONLINE. Report Z3748.00, WL, Delft Hydraulics.

van Rijn, L. C. (2007a). Unified view of sediment transport by currents and waves. I: Initiation of motion, bed roughness, and bed-load transport. *Journal of Hydraulic Engineering*, 133(6), 649–667. https://doi.org/10.1061/(ASCE)0733-9429(2007)133:6(649

van Rijn, L. C. (2007b). Unified view of sediment transport by currents and waves. II: Suspended transport. *Journal of Hydraulic Engineering*, 133(6), 668–689. https://doi.org/10.1061/(ASCE)0733-9429(2007)133:6(668

Vieira da Silva, G., Toldo, E. E., Klein, A. H. d. F., Short, A. D. (2018). The influence of wave-, wind- and tide-forced currents on headland sand bypassing – Study case: Santa Catarina Island north shore, Brazil. *Geomorphology*, *312*, 1–11. https://doi.org/10.1016/j.geomorph.2018.03.026

Vieira da Silva, G., Toldo, E. E., Klein, A. H. d. F., Short, A. D., Woodroffe, C. D. (2016). Headland sand bypassing - Quantification of net sediment transport in embayed beaches, Santa Catarina Island North Shore, Southern Brazil. *Marine Geology*, *379*, 13–27. https://doi.org/10.1016/j.margeo.2016.05.008